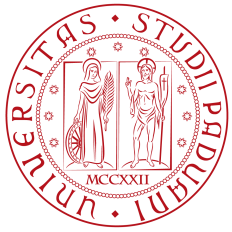

UNIVERSITÀ DEGLI STUDI DI PADOVA

Dipartimento di Fisica e Astronomia "Galileo Galilei"

Corso di Laurea in Fisica

Tesi di Laurea

Preparation of the measurement system for the spatial characterization of SPIDER negative-ion plasma source

Relatore

Dr. Gianluigi Serianni

Correlatore

Dr. Emanuele Sartori

Laureanda

Beatrice Segalini

Matricola 1151796

Anno Accademico 2018/2019

Beatrice Segalini, University of Padova
A.A. 2018-2019

Abstract

Neutral beam injectors are fundamental auxiliary heating systems for nuclear fusion machines.

The formation of the negative-ion beam, precursor of the neutral beam, occurs by extracting the ions from a plasma through a multi-aperture, multi-electrode electrostatic accelerator. In the case of the ITER neutral beam injector, to obtain sufficient current, the extraction takes place through 1280 openings distributed over a very large area, which must be illuminated by a sufficiently uniform plasma.

The plasma, formed in 8 radio-frequency drivers, passes through an expansion chamber before reaching the extractor. The experimental study of the plasma parameters at the location of the ion extraction, and of its expansion from the driver region, is possible using Langmuir probes on mobile supports.

In this dissertation, a preparatory study is conducted for characterizing negative ion plasma in SPIDER negative-ion plasma source. A bibliographic research is performed in order to understand how similar measures were taken in the past in similar devices, at the end of which three different kind of probes are designed and tested: a Mach probe, a double Langmuir probe and a planar Langmuir probe.

The Mach probe is composed of 4 cylindrical pins and is designed in order to measure plasma flux and velocity drift. It was tested by assembling it on a rotating system inside an Argon plasma, in order to verify its symmetry and if it is suitable for an RF source like SPIDER.

Next, the double probe (named ADEL, i.e. A Double Electrode Langmuir probe) consists of two parallel cylindrical electrodes, and it should give a completely floating measures of the plasma parameters. It was tested inside the CRISPy experiment (Compact RF Ion Source Prototype for emittance scanner testing) in order to give an estimate of electron temperature and plasma density.

Regarding the planar Langmuir probe, it is composed of two electrodes: a main electrode and a compensation one. A model in LTSpice is used to simulate its behaviour in an RF plasma, so as to find the optimum capacity to be put in parallel between the two electrodes.

Finally, a plan for probes installation and measurements in SPIDER is established in light of the results obtained.

Contents

Listing of figures

1

Introduction

ITER AND SPIDER The ITER Neutral Beam Test Facility (NBTF), called PRIMA (Padova Research on ITER Megavolt Accelerator), is hosted in Padova and includes two experiments: MITICA (Megavolt ITER Injector Concept Advancement), the full-scale prototype of the ITER heating neutral beam injector (HNB), and SPIDER (Source for Production of Ion of Deuterium Extracted from RF plasma), the full-size radio frequency negative-ions source, which shall provide confirmations and key information before the construction of the corresponding components in ITER.

The realization of these experiments has been recognized as necessary to make the future operation of the ITER heating neutral beam injectors efficient and reliable, fundamental to the achievement of thermonuclear-relevant plasma parameters in ITER.

	Unit	H	D
Beam energy	keV	100	100
Max beam source filling pressure	Pa	0.3	0.3
Max deviation from uniformity	%	± 10	± 10
Current density of ions extracted from the plasma	Am^{-2}	> 355	> 285
Beam on time	s	3600	3600
Co-extracted electron fraction (e−/H−) and (e−/D−)		< 0.5	< 1

Table 1.1: SPIDER requirements for ITER.

Focusing on SPIDER, its main purpose is to optimize the performance of an ITER HNB-like negative ion source by maximizing the extracted negative ion current density and its spatial uniformity and by minimizing the ratio of co-extracted electrons, in order to match the ITER requirements, shown in Table 1.1 [1].

The target NI current in deuterium at the extraction was calculated from the desired neutral beam current at the tokamak port, and proceeding backwards considering the beam losses in the beamline, neutraliser and all along to the extraction region of the electrostatic accelerator.

The part which is of interest in this dissertation is the RF ion source (see Figure 1.2 [2]). It is a complex chamber, featuring a main space, enclosed in a structure called source case and facing the plasma grid, on whose surface most of negative ions are generated, and eight rear smaller chambers called drivers, where the gas is injected (hydrogen or deuterium). RF coils wound around the lateral wall of the drivers, and connected to a 1 MHz oscillator, transfer the RF power and ionize the gas: the resulting plasma flows then into the main chamber, where the additional presence of caesium enhances the number of negative ions generated on the surface of the plasma grid, as it could be seen in Figure 1.1.

The nominal power of the RF generators is 800 kW for the whole ion source, composed by 8 drivers.

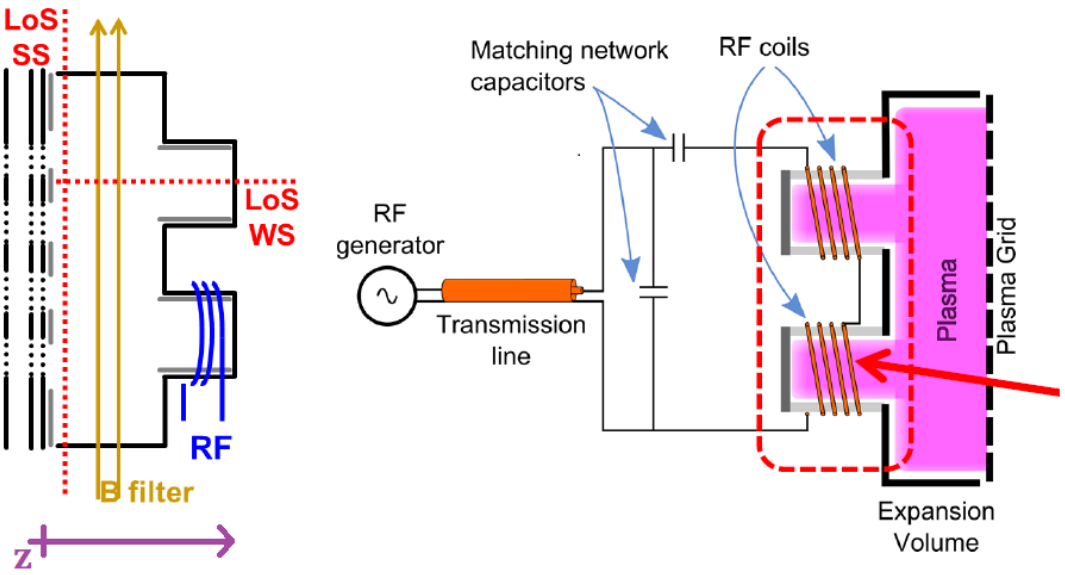

Figure 1.1: Simple circuit scheme of RF source and expansion chamber in SPIDER.

The RF ion source also includes a series of auxiliary systems (see [2] and references), such as the electric circuits for power input, the cooling circuits for heated components, the gas supply system, three ovens to dispense the caesium inside the source, starter filaments to initiate the plasma and several diagnostic sensors to monitor and control the source behaviour. Ports are foreseen on the surface of several elements, in order to allow the connection of the auxiliary systems and the diagnostic accesses.

In Figures 1.3, a detailed view of SPIDER's RF ion source components.

Aim of the thesis This work focuses on the design of a diagnostic system composed of different types of Langmuir probes, aimed at characterizing SPIDER's plasma. The probes will be positioned inside the experiment with metal moving supports, like in Figure 1.4.

The final goal is to have a detailed idea of how each type of probe works, what are their limits and how they could be used in view of SPIDER's future measurements.

This thesis is organised as follows. A bibliographic review is provided in Chapter 2, to

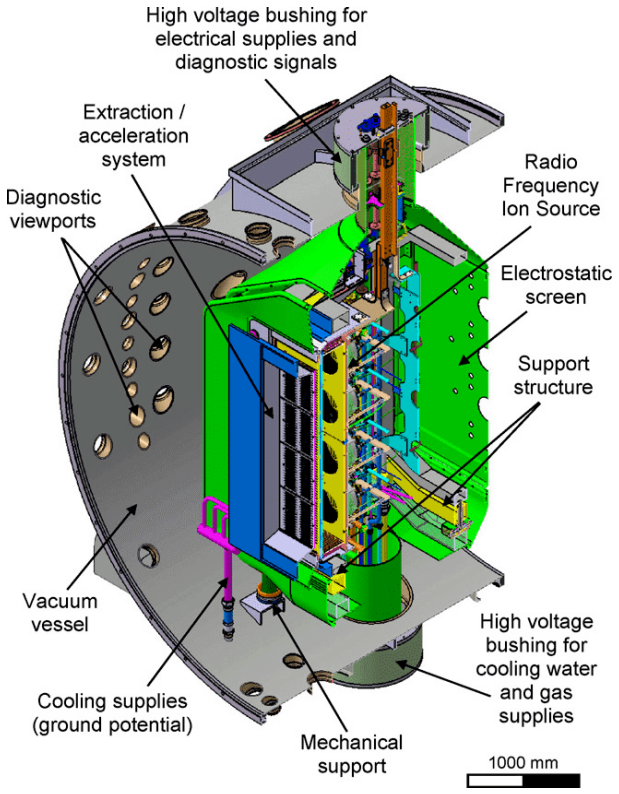

Figure 1.2: Overall section view of the SPIDER beam source.[2]

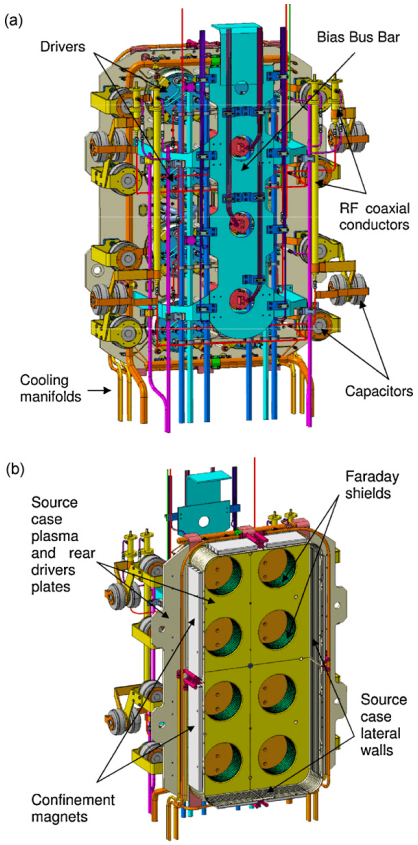

Figure 1.3: RF ion source: (a) rear view; (b) front view.[2]

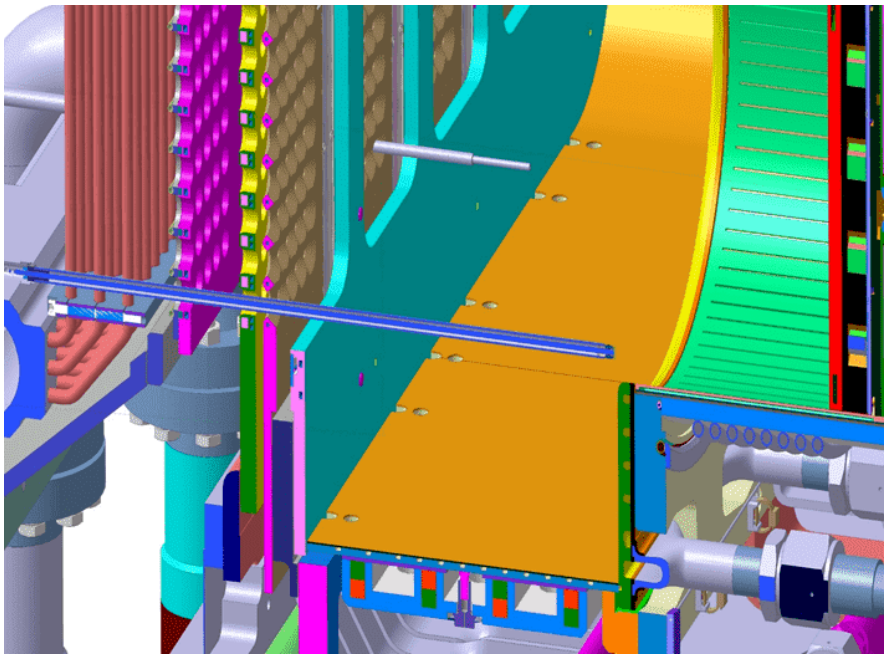

Figure 1.4: Diagram of possible probe positioning inside SPIDER's main plasma chamber.

identify the peculiarities of similar works in order to provide solid basis to the design of the experimental setup for SPIDER. Chapter 3 describes design and following calibration of a four pin Mach probe. The next chapter, instead, describes a double electrode Langmuir probe, which collects totally floating data and is tested specifically to see its effectiveness in a RF ion source. Chapter 5 contains details on the project of some planar Langmuir probes. Some LTSpice simulations and their analysis is conducted in order to predict their behaviour in a RF plasma.

In Chapter 6, a plan for probes installation and measurements in SPIDER is established in light of the results obtained. Finally, Chapter 7 includes the conclusions.

If we knew what it was we were doing, it would not be called research, would it?

Albert Einstein

2

Theoretical overview

2.1 Negative ion sources

Before starting analysing the diagnostic system designed, it is important to clear some major physical aspects of negative ion sources, such as SPIDER, which are thoroughly described in [3] and references.

Using negative ion sources is preferred because only through them the conditions of Table 1.1 could be reached.

In fact, the adsorption length for neutral beam ionization in a plasma is roughly

$$\lambda = \frac{E}{18 \cdot n \cdot \mathcal{M}}$$

with λ in m, n in $10^{19}\mathrm{m}^{-3}$, m_i in u, E in keV. Depending on the plasma minor diameter and

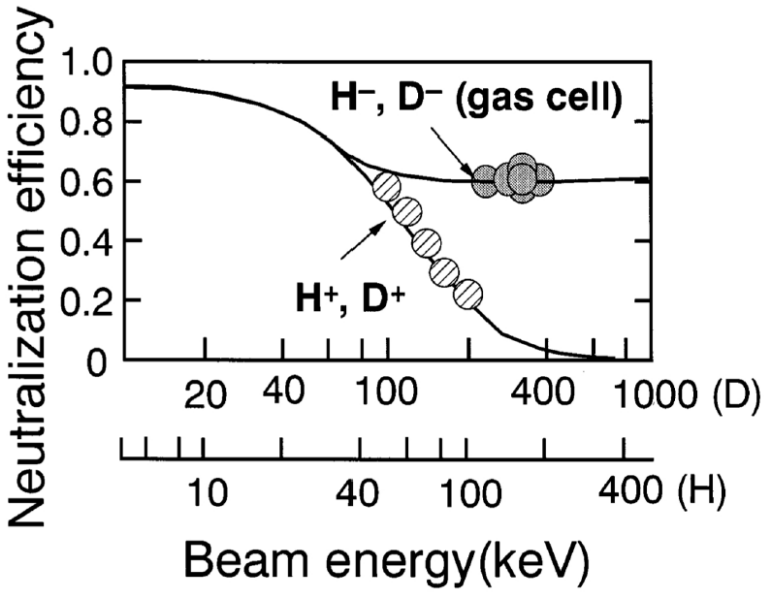

Figure 2.1: Maximum neutralisation efficiency of a fast D ion beam in a gas cell, as a function of the ion energy.[4]

density, a minimum particle energy can be defined for the neutral beam, in order to deposit a sufficient power on the plasma core rather than to the plasma edge. The required fast neutral energy gets in the range of 1 MeV. With this energy, it is increasingly difficult to obtain fast hydrogen atoms starting from precursor beams composed of positive ions (Figure 2.1). For that reason, recent and future heating neutral beams will be based on negative ion beams. In the interaction with background gas, which is basically the common strategy to neutralise the precursor ion beam, it is much easier to detach the extra-electron from a negative ion (H- has a binding energy of 0.75 eV and a very large cross-section for electron detachment in this energy range) rather than to attach one electron to a positive ion.

These are two main issues concerning negative ions: first, the formation of negative ions is not so probable in a hydrogen plasma discharge, and a method to increase their density is necessary to provide a sufficient beam current; secondly, that they are (obviously) negatively charged particles, as are electrons, which are therefore co-extracted together with the negative

ions by the electrostatic accelerator. They have a very small mass compared with that of ions and they should not be accelerated to full energy in the accelerator, to avoid dissipation of electrical power but especially to avoid damaging the beamline components with stray energetic electrons.

The two major negative hydrogen ion formation processes are surface and volume production.

Volume production occurs mainly in sources producing negative ions in the volume of weakly ionised molecular gases (hydrogen, deuterium). It is generally accepted that this production is due to dissociative attachment of low energy electrons to rovibrationally excited molecules.

The main negative hydrogen ion formation process in pure hydrogen plasma is dissociative electron attachment to highly rovibrationally excited molecules: low energy electrons can be very effective in generating H- ions by this process. On the other hand, more energetic electrons are necessary to create highly vibrationally excited molecules; therefore the volume production is a two-step process which can be optimised by separating the plasma into two regions, one with high electron temperature where excited molecules are produced, and one region close to the extraction where excited molecules are dissociated by a low-temperature electron population. This scheme can be obtained by separating the two plasma regions by a a transverse magnetic field, featuring a much reduced perpendicular diffusivity for high-energy tail of the electron energy distribution function [3].

Besides, three volume destruction processes also exist: mutual neutralization in collision with positive ions, electron detachment in collision with electrons, and associative detachment in collision with atoms. Among the H- ion destruction processes the most important one is mutual neutralization.

For what concern surface production, two types of H- ion emissions from a surface are

present: thermodynamic equilibrium surface ionization and non-thermodynamic equilibrium surface ionization (or secondary negative ion formation) processes.

In the case of thermodynamic equilibrium surface ionization, atoms impinging on a hot metal surface may be emitted as atoms or ions in subsequent evaporation processes after mean residence times long enough for the establishment of equilibrium. In this case the probability of leaving the hot surface as a negative ion depends on the difference between the electron affinity and the work function, φ, of the surface and is given by the Langmuir–Saha relation. A low work function surface is required for negative ion formation.

However the H- ion emission from surfaces in surface plasma sources is the result of the interaction of a fast particle with the surface and is a non-equilibrium one. It may be obtained even from a surface with comparatively high work function, but no investigations of this phenomenon were reported.

Efficiency of H-/D- ion generation could be enhanced by adding caesium. This is caused by a substantial increase in the secondary emission of negative ions from the electrode bombarded by plasma particles. Caesium adsorption lowers the surface work function and this increases the probability of sputtered particles escaping in the form of negative ions. This probability increases with the decrease in work function and the increase in velocity of particles moving away from the electrode surface.

In a electronegative plasma, the interpretation of electrostatic probe characteristics if not straightforward. Given these facts, the need for diagnostics specifically for negative ions plasmas is justified.

2.2 General information on Langmuir probes

Plasma diagnostics must serve a wide variety of roles. On the one hand, for applications in basic plasma experiments, they are needed to determine the details of the electron and

ion distribution functions. In fusion experiments, just like SPIDER, they are required to determine moments of the distribution functions such as temperature. On the other hand, in plasma processing control, they may be needed to just give an indication that a plasma processing device has the same plasma characteristics as on a previous occasion, but it may not be necessary to know the characteristics.

Perhaps the simplest of all plasma diagnostic techniques involves the insertion of a solid object into the plasma and the measurement of the particle and energy fluxes to the object, i.e., a probe, objects which must serve a wide variety of roles.

The most common type of diagnostic are Langmuir probes, which have been used to serve the full range of roles over a wide range of plasma densities, from a few particles per cm^3 to greater than $10^{14} cm^{-3}$.

Langmuir probes are often used as plasma diagnostics because of their relative ease to construct. They measure electrical currents which depend on their bias voltage with respect to the plasma potential. A very simple scheme of a probe in the plasma is shown in Figure 2.2. Over a very wide range of situations, the details of the current-voltage I vs. V characteristics can be related to the plasma parameters that are present in the absence of the probe.

Although probes perturb their local surroundings (and this nevertheless complicates the interpretation of Langmuir probe characteristics), it is still possible to determine electron temperature T_e, electron density n_e, plasma potential V_p, and electron and ion beam energy over an extremely wide range of parameters.

Broadly speaking, if it is hypothesized the electrons to be Maxwellian and non-drifting, which is a common yet effective assumption, the probe current I_e could be written ([5], (12) formula):

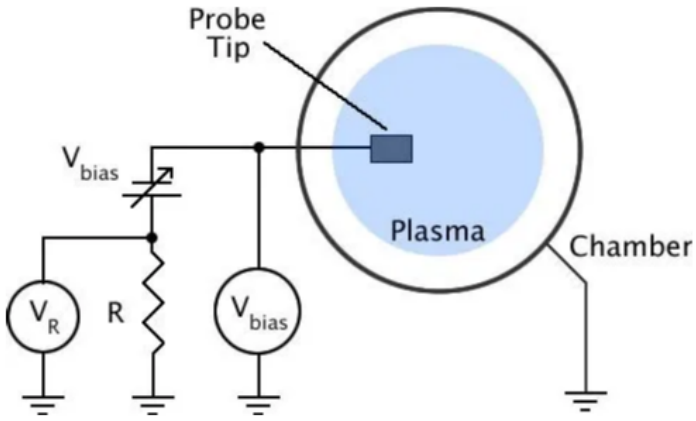

Figure 2.2: Simple circuit diagram of a general Langmuir probe setup, source: https://www.davidpace.com/example-of-langmuir-probe-analysis/.

$$I_e(V) = I_{e,sat} \exp \frac{-e(V_p - V)}{k_B T_e}, V \leq V_p$$

$$I_e = I_{e,sat}, V > V_p$$

where $I_{e,sat} = S n_{e,\infty} e \sqrt{T_e / 2\pi m_e}$ is commonly referred to as the electron saturation current, $n_{e,\infty}$ is the plasma electron density, and S is the collecting area of the probe.

The total current to the probe is the sum of the electron and the ion current. The ion saturation current could be estimated in the same way as the upper formula only if ion temperature is comparable with electron temperature (i.e., in fusion plasmas or in thermal plasma processing plasmas). In the most common case of $T_e \gg T_i$ the ion saturation current is given by the Bohm current ([5], (29) formula):

$$I_{i,sat} \simeq 0.6 n_{i,\infty} S \sqrt{\frac{T_e}{m_i}}$$

where m_i is the ion mass. For further information on the interpretation of Langmuir probes data, see [6].

2.3 Previous measurements taken

One of the key issues considered in the development of negative ion sources is the transverse magnetic filter field, which separates the hot plasma generation region (electron temperature $\approx$ 10 eV) from the cold plasma close to the extraction region ($\approx$ 1 eV) and is exhaustively studied in [7].

In the negative ion sources for fusion the filter field has three different tasks. First of all it cools the electrons down to minimize the destruction of negative ions by collisions with electrons, which is important for enhancing the negative ion production by dissociative electron attachment to rovibrationally excited hydrogen molecules, and for electron stripping to become negligible as destruction mechanism.

Secondly, the number of co-extracted electrons is reduced by the filter field due to the reduced electron temperature and density and, thirdly, it increases the extraction probability for the surface produced negative ions which are bent back from the surface to the extraction apertures by the magnetic field.

On the other hand, the transverse magnetic field causes plasma drifts resulting in non-uniform plasma illumination of the extraction area which can have consequences for the beam homogeneity. Thus, the magnetic filter field plays a crucial role for the source performance.

Prove of these phenomena were collected by a system of two Langmuir probes in the IPP prototype source, an example of the complex magnetic field map in the source and the variation of the horizontal component of the magnet field in the axial direction with position of the frame are given in Figure 2.3.

The plasma parameters obtained without magnetic filter field and with the filter frame in the closest distance to the plasma grid as possible, i.e. the $z = 9$ cm position, are plotted

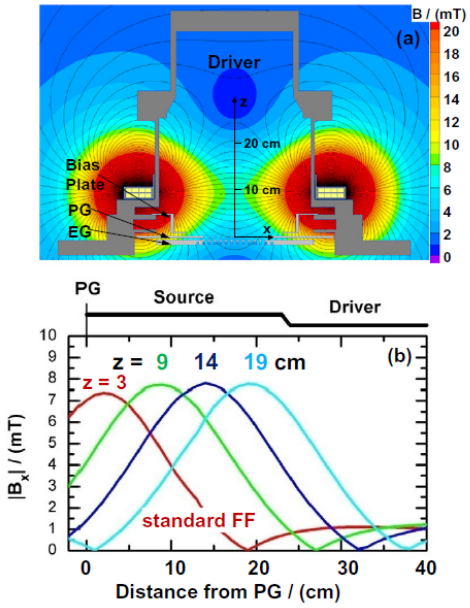

Figure 2.3: On top, structure of the magnetic field generated with the filter frame at position $z = 9\,\mathrm{cm}$ $(y = 0)$. Bottom pic: strength of the horizontal magnetic filter field in the axial direction for different positions of the filter frame and for the internal magnets in the standard configuration $(x = y = 0)$.

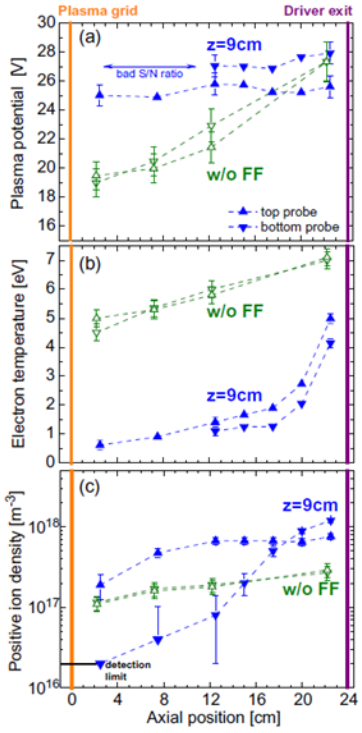

Figure 2.4: Plasma parameters in the axial direction as measured by the Langmuir probes in the IPP prototype source with the flexible filter frame at $z = 9\,\mathrm{cm}$ with a very low amount of caesium in the source and without filter field. Both measurements are carried out at $0.6\,\mathrm{Pa}$ filling pressure and $40\,\mathrm{kW}$ RF power.

in Figure 2.4. As expected the electron temperature is drastically reduced close to the extraction system by the influence of the magnetic filter. The field strength is sufficient to achieve temperatures well below the desired 2 eV.

A comparison of the profile of the electron temperature (Figure 2.4(b)) with the profile of the magnetic field (Figure 2.3(b)) suggests that the increasing part of the filter field strength along the flux of the electrons from the driver towards the grid is predominantly responsible for the electron cooling. The profile of the plasma potential is less pronounced with magnetic field. The plasma density shows higher values close to the driver compared with the measurements without filter and the plasma symmetry is strongly distorted by the magnetic field.

In order to study the influence of the magnetic filter field on the plasma flowing out of the driver, in [7] the Langmuir probes are kept at fixed position (close to the driver exit at $z = 20\,\mathrm{cm}$) and the position of the magnetic filter field is varied. Figure 2.5 shows that the asymmetry in the plasma density and in the plasma potential increases with increasing z-position of the magnetic frame.

Finally, Figure 2.6 shows the influence of caesium on the axial profiles. The plasma potential is remarkably reduced by caesium, i.e. the *IV* characteristic is basically shifted to lower voltages. A change in the electron temperature is not observed. The plasma density, however, seems to be lower at the driver exit than without caesium and the plasma symmetry is also improved.

The influence of the magnetic field position on the plasma parameters derived from Langmuir probe measurements in the expansion chamber of the IPP RF negative ion source was examined in [8]. The use of two movable Langmuir probes showed a strong and quite unexpected plasma inhomogeneity between the top and bottom parts of the expansion chamber. The strongest inhomogeneity between top and bottom plasma parameters was observed to

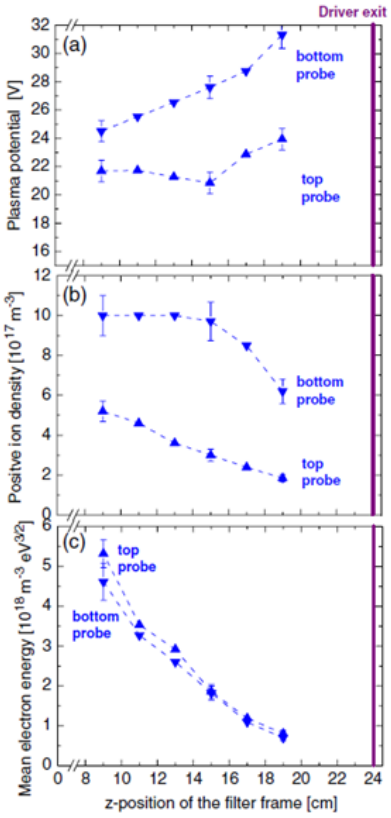

Figure 2.5: Plasma parameters in the IPP prototype source at fixed position of the Langmuir probes ($z = 20$ cm) for different positions of the filter frame at 0.6 Pa filling pressure and 40 kW RF power with a very low amount of caesium in the source.

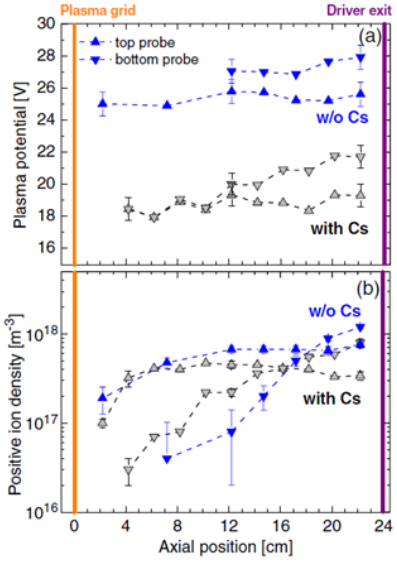

Figure 2.6: Plasma potential and positive ion density as measured by the Langmuir probes in the IPP prototype source in the axial direction with the filter frame at $z = 9$ cm at 0.6 Pa filling pressure and 40 kW RF power with and without evaporation of caesium in hydrogen discharges.

be at the driver exit: this is clear if Figure 2.7 and 2.8 are compared. It is a reasonable assumption that the interaction of several cross-B drift plays a key role in producing this inhomogeneity. When the magnetic field is present, the observation of the plasma inhomogeneity right at the driver exit suggests that despite the energy of the driver being coupled into the plasma uniformly, the potentials, temperatures and densities could show a significant difference between the top and bottom parts of it.

A further study on the effect of different gasses on plasma parameters is conducted by McNeely et al. in [9], with the same plasma source.

Adding argon to the source resulted in an immediate increase in the positive ion density, but no change in either the electron temperature or the plasma potential. When argon is added and its concentration is $> 10\%$ then the n_e is enhanced in the bulk region of the source. However, near the extraction grid there is no significant increase in the density, as can be seen in Figure 2.9. Figure 2.10 shows that the effect of adding argon on the values of $\langle E \rangle$ is at best minimal. There is some small change near the grid but this is within experimental error. The most significant change is that of the plasma potential, where in the bulk it increases by 15% but this difference vanishes as the probe approaches the grid.

Adding caesium by seeding has proved to have a very similar effect (Figure 2.11 and 2.12).

Another interesting feature of [9] analysis is the introduction of a Faraday shield. Its implementation was necessary to increase the pulse length of the source, to protect the probe from sputtering and to prevent thermal failure. For the case of a pure hydrogen plasma comparing equivalent measurements with and without the Faraday screen are shown in Figures 2.13 and 2.14.

It can be seen that the electron density is enhanced by nearly a factor of 2. The values of $\langle E \rangle$ with the Faraday screen seem to be slightly lower in the bulk but increased near the grid. The biggest difference is in the values of U_{pl}. The plasma potential with the Faraday screen is

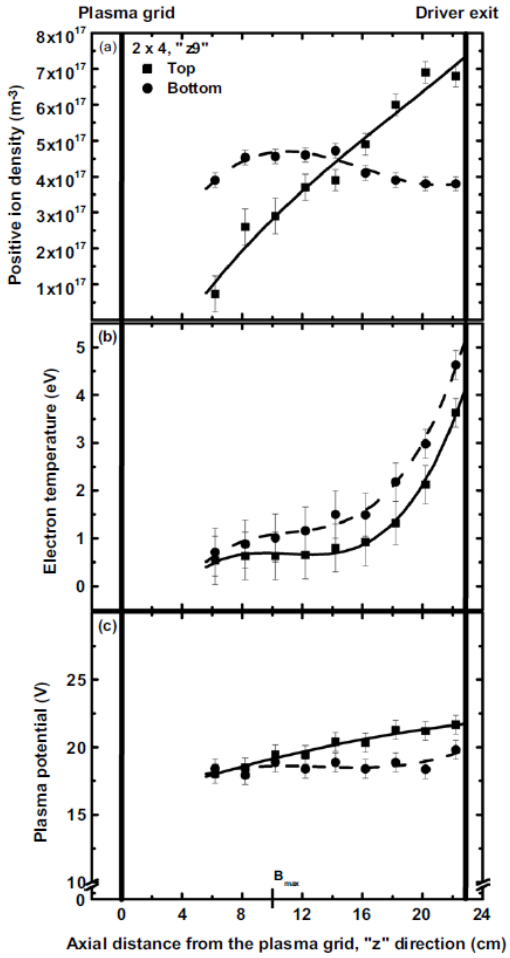

Figure 2.7: (a), (b) and (c) represent the variations of the positive ion density, electron temperatures and plasma potential for the two Langmuir probes, moving along the expansion chamber and for the magnetic field filter positioned at 9 cm from the plasma grid. Straight and dashed lines refer to the top and bottom probe, respectively. The position of the maximum magnetic field strength is indicated.

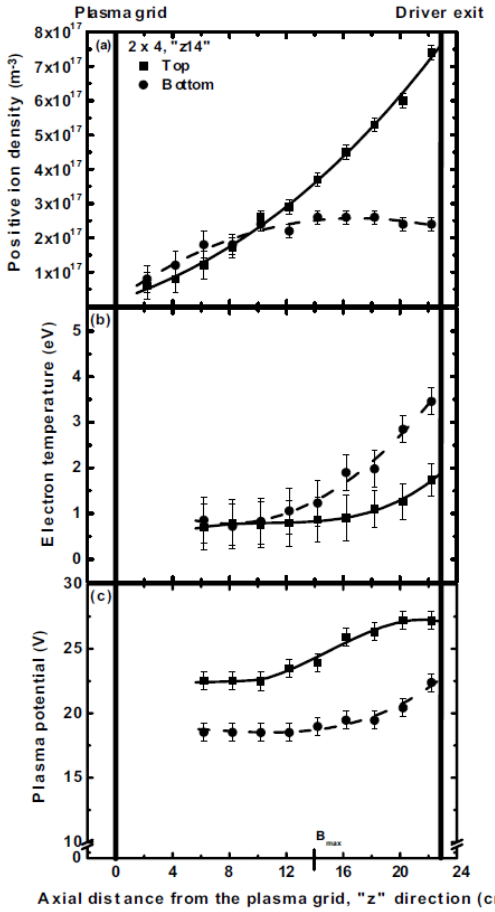

Figure 2.8: (a), (b) and (c) represent the variations of the positive ion density, electron temperatures and plasma potential for the two Langmuir probes, moving along the expansion chamber and for the magnetic field filter positioned at 9 cm from the plasma grid. Straight and dashed lines refer to the top and bottom probe, respectively. For the positions $z = 2$ and 4, only the positive ion density could be derived via the Chen formula due to a poor signal-to-noise ratio in the electron branch. The position of the maximum magnetic field strength is indicated.

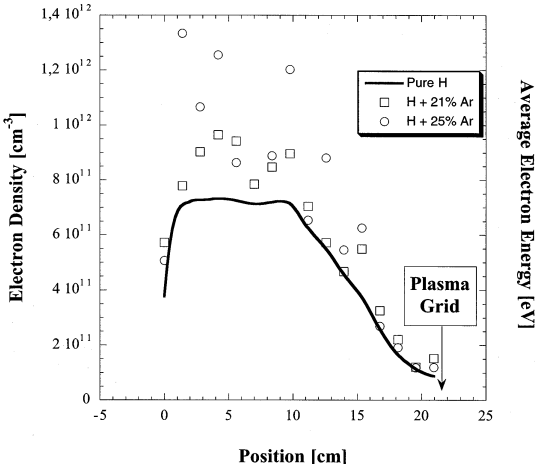

Figure 2.9: The effect of adding argon to a hydrogen plasma on the electron density. The source pressure is 0.5 Pa.

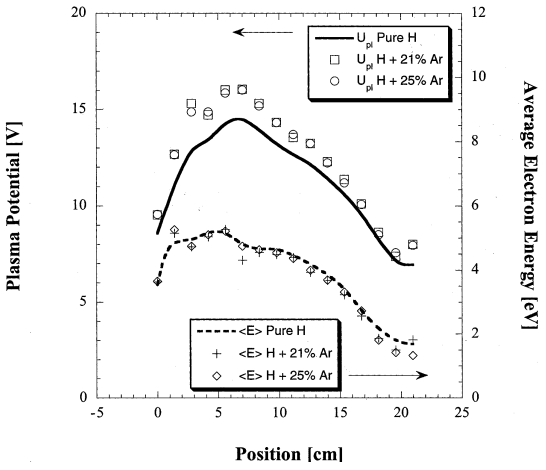

Figure 2.10: The effect of adding argon to a hydrogen plasma on the average electron energy and plasma potential. The source pressure is 0.5 Pa.

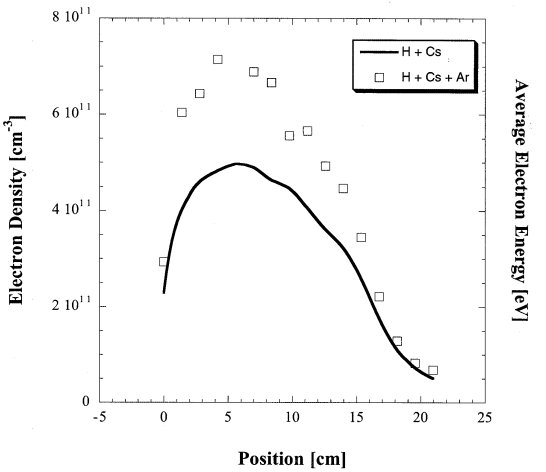

Figure 2.11: Mean values for electron density from 12 (4 without Ar, 8 with Ar) scans are compared to show the effect of adding argon on a caesium seeded hydrogen plasma at source pressure 0.5 Pa.

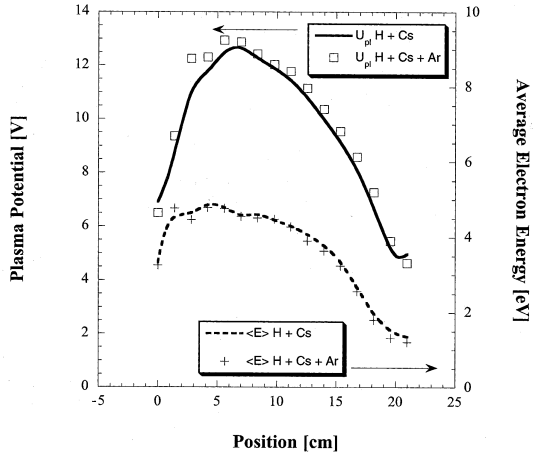

Figure 2.12: Mean values for average electron energy and plasma potential from 12 (4 without Ar, 8 with Ar) scans are compared to show the effect of adding argon on a cesium seeded hydrogen plasma at source pressure 0.5 Pa.

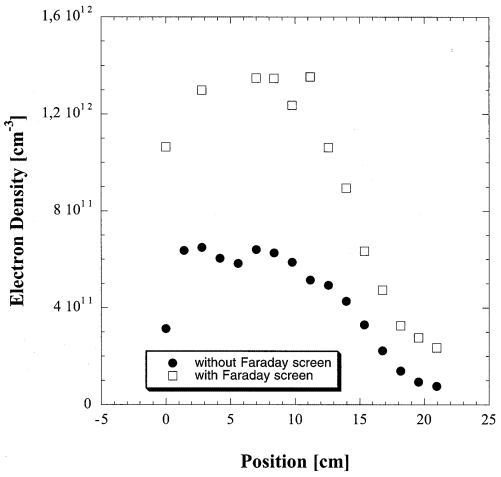

Figure 2.13: The effect on the electron density of adding a Faraday screen to the Type VI source for a pure hydrogen plasma with source pressure 0.5 Pa and an applied RF power of 55 kW.

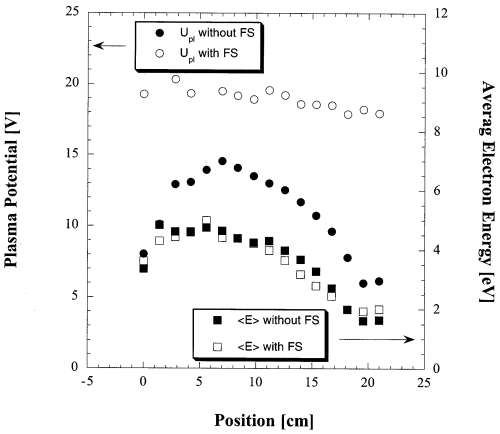

Figure 2.14: The effect on the average electron energy and plasma potential of adding a Faraday screen to the Type VI source for a pure hydrogen plasma with source pressure 0.5 Pa and an applied RF power of 55 kW.

much higher (between 35 and 170% higher) and the shape is much flatter; not following the shape of the electron temperature at all. A possible explanation for this effect is due to the fact that the Faraday screen is electrically connected to the backplate of the driver, which is in turn connected to the rest of the source body.

Calculating electron energy distribution function could also be valuable for properly understanding the plasma's characteristics.

In [10], a Langmuir probe system capable of directly measuring the 2nd derivative of the I–V trace has been developed and tested in the KAMABOKO III source. The probe system is also capable of analysing the I–V trace using a variety of common procedures (Figure 2.15).

Plasma parameters in the KAMABOKO III source were determined and the electron energy distribution function (EEDF) was found to be non-Maxwellian with an effective electron temperature higher than the inferred Maxwellian temperature, with all the consequences related to the case. Hence, to model and optimize the production of negative ions, it is clearly necessary to know the form of the EEDF.

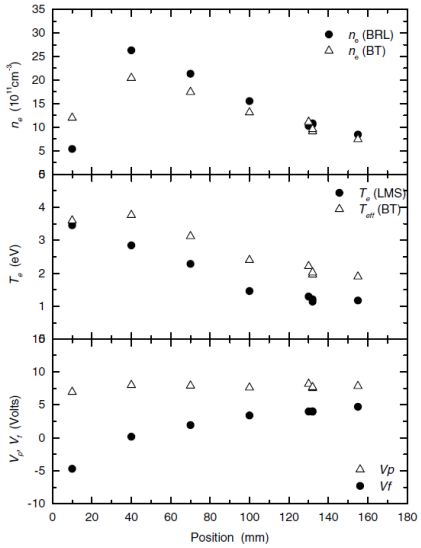

Figure 2.15: Plasma parameters as a function of position from the edge to the centre of the source. The arc power was 47 kW and the pressure was 0.3 Pa.

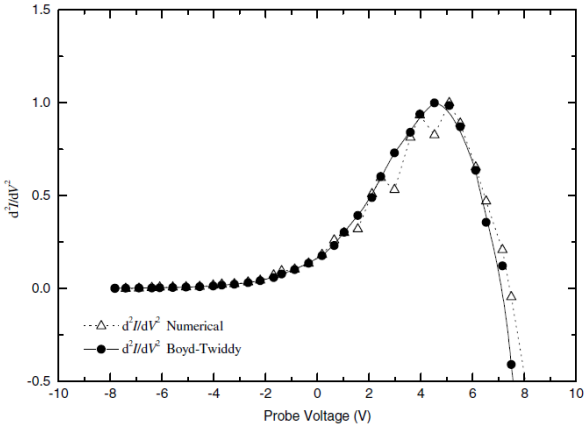

Figure 2.16: 2nd derivative of the I–V curve showing the numerical and BT method. Measurement taken at the centre of the discharge with arc power is 47 kW and the pressure was 0.3 Pa.

The EEDF was determined by both numerical differentiation and the direct 2nd derivative (Boyd–Twiddy) method have been compared (Figure 2.16). Both methods gave a similar form for the EEDF but the form of the numerical method depended on the smoothing method employed. Since the degree of departure of the EEDF from Maxwellian may not be known, measuring the EEDF is the most reliable way to use the Langmuir probe diagnostic, which would so gives more trustworthy results.

Furthermore, plasma flux could also be measured through a Mach probe: an example of this kind of measures could be find in [11]. In this thesis, the Mach probe used was designed starting from the one in the article, shown in Figure 2.17.

It has been shown that the plasma flow velocity can approach Mach number of 1 and it is strongly dependent on the transverse magnetic fields. The measurements done in BATMAN ion source using a Mach probe along the axis comprehend plasma density, plasma potential, electron temperature, and the barometrically measured background gas pressure

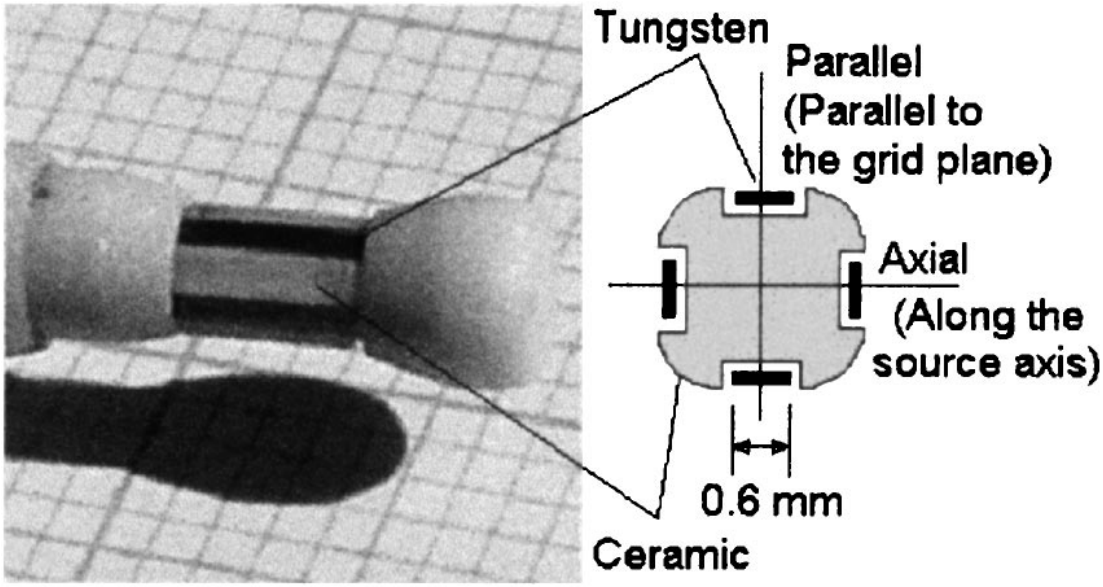

Figure 2.17: Picture and schematic diagram of the Mach probe with two orthogonal heads.

(Figure 2.18).

The analysis in [11] shows that plasma flow is an important characteristic of a plasma source where a large gradient of plasma potential exists. The collisions between the plasma ions and the background gas molecules create a pressure gradient along the flow direction. This pressure gradient along the axis is proportional to the radio frequency power and the filling gas pressure. Presence of transverse magnetic filter reduces the plasma flow velocity, which could affect the negative ion production on the caesiated grid surface, given that the surface production of negative ions also depends on the flux of the positive ions and energetic atoms impinging the surface.

Finally, one could ask whether or not a presence of a proton flux is relevant to the estimate of plasma parameters. This issue is of high relevance for further analysis of the negative hydrogen ion production on the plasma grid surface as well as the ion transport and beam formation and is analysed in [12], where a Monte Carlo code, `ProtonFlow3D` is described and used to calculate the energy distribution of the protons impinging the plasma grid surface

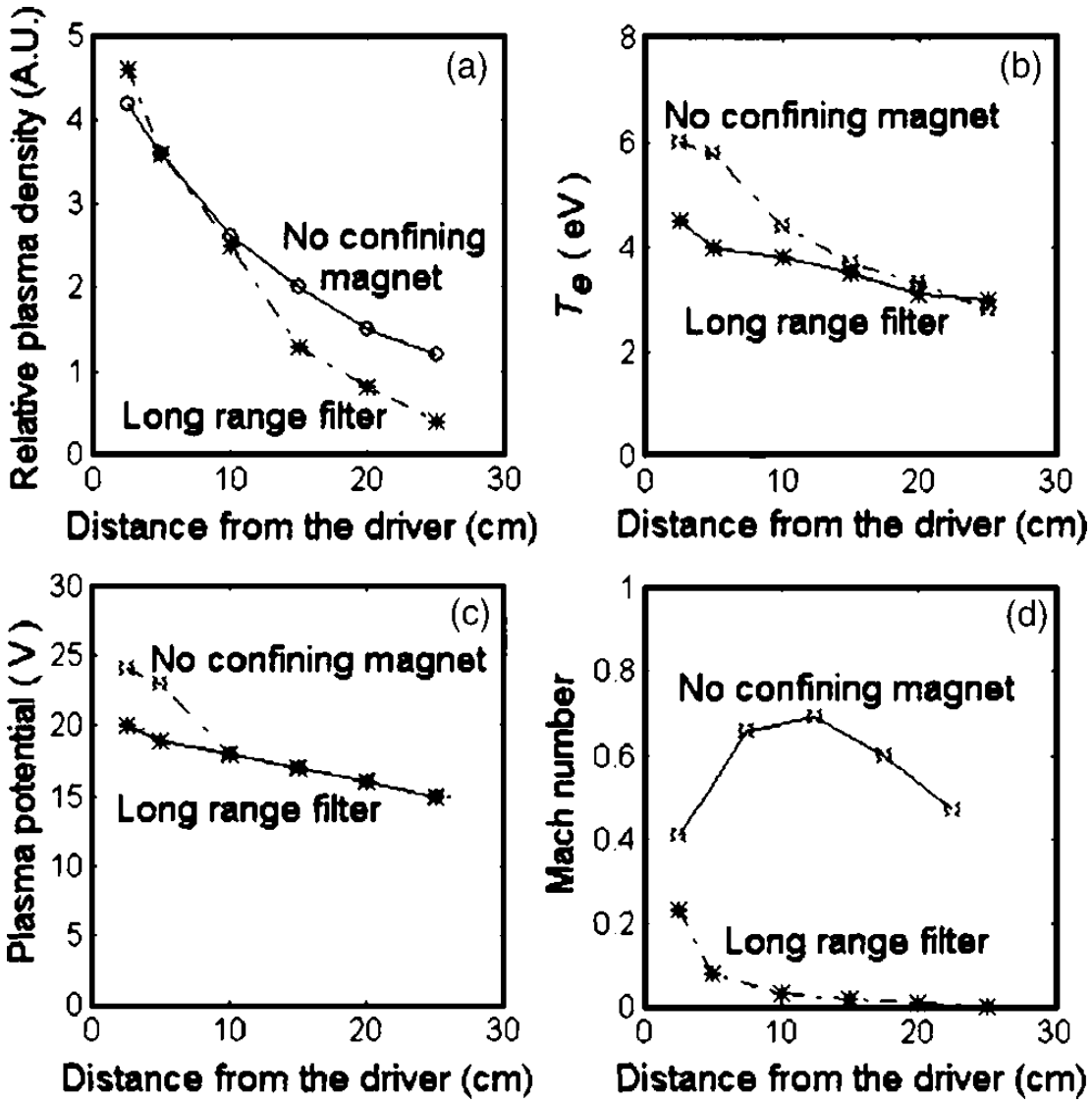

Figure 2.18: Relative plasma parameters and plasma flow for two different source configurations (one with a strong transverse magnetic filter applied along the y axis of the reference frame, the other without).

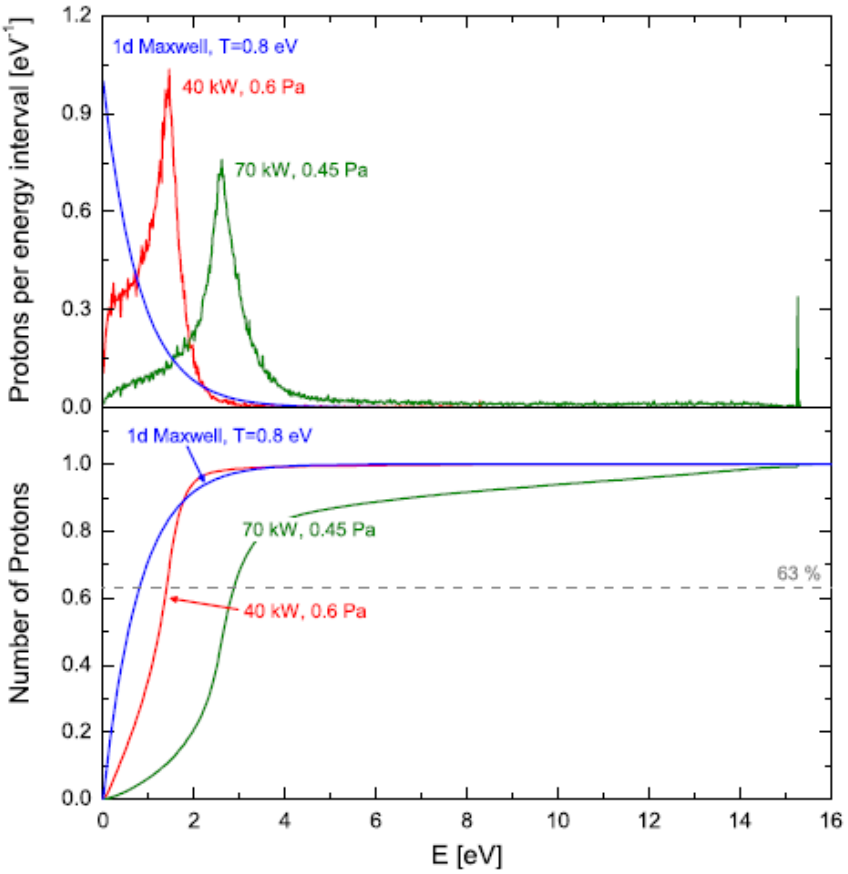

Figure 2.19: Energy distribution of the protons impinging the plasma grid surface (top). Integrated energy distribution (bottom).

(Figure 2.19). It can be stated that the conversion of positive hydrogen ions to negative ions at the surface of the plasma grid is not the dominant process over the conversion of hydrogen atoms.

Knowledge and error flow from the same mental sources;
only success can tell one from the other.

Ernst Mach

3

Four pins Mach probe

The first probe analized was a Mach probe. It was relevant to test and verify its main properties in order to evaluate if it could be of use in the characterization of SPIDER plasma source.

If correctly calibrated, the probe could be used to measure electron drift velocity, which would add information to the characterisation of SPIDER's plasma. To obtain valuable result, however, it is needed to check the collecting areas of the four electrodes, and verify if there are any geometrical asymmetries in the probe.

The probe has been tested twice in ATHENIS [13], an experiment in Consorzio RFX, in two different versions.

Settings The first probe is shown in Figure 3.1. It is composed of four cylindrical tungsten electrodes, each one 5 mm long and with 0.8 mm of diameter. The four pins are kept in place by five alumina cylinders, welded with ceramic glue on the top of the probe and stuck in an alumina base. The four electrodes are named like the four cardinal points, as shown schematically in Figure 3.2. There is also a reference electrode, which can be also seen in 3.1: it is a thin foil of tungsten covering the base of the probe.

In Figure 3.3, besides, you could find the scheme of the electronic connectors. In fact, each electrode is tinned to a copper wire, properly shielded, and then attached to a female-female junction, whose air-side is shown in the previously mentioned picture. Each letter in 3.3 represent an electrode, letter X is the reference one. The wires are connected to some shunt resistances ($R_{shunt} = 448(5)\ \Omega$) before being attached to the acquisition system (DL716 Yokogawa 16 channels digital scope). The plasma in which the probe worked was an Argon plasma ($m_i = 6.6335 \cdot 10^{-26}$kg).

The whole probe, complete with cables, is bound to a support which allow rotation around its main axis. A rudimentary angular positioning system was built for taking the first sets of measures, in order not to lose track of which electrode is which while the probe is installed in the experiment.

In the next two figures (3.4, 3.5), the positioning inside the experiment is presented, from two different points of view. In both pictures the plasma is on and can be clearly seen on the filament on top.

Calibration and full rotation of the probe With these settings, some measurements were taken, despite some technical problems. In fact, in the first sets the North elec-

Figure 3.1: First prototype of the Mach probe, with cables and metal rotating support.

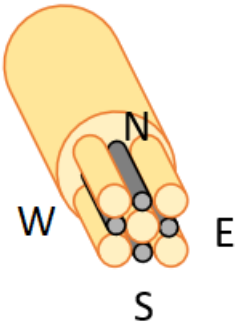

Figure 3.2: Electrodes positioning and labelling.

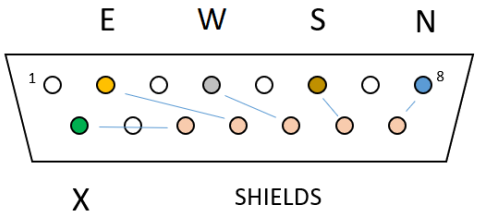

Figure 3.3: Female connectors scheme for the cables linked to the electrodes, air side.

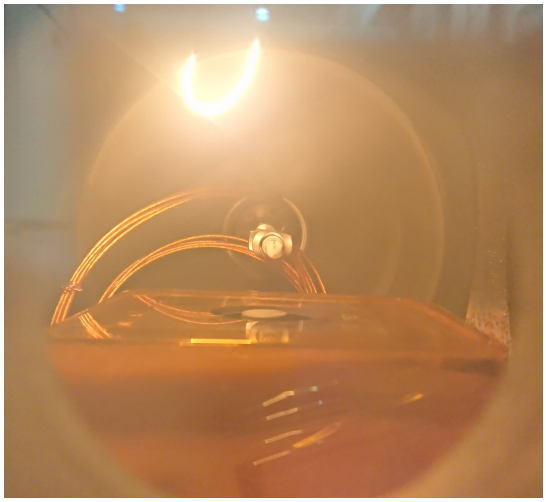

Figure 3.4: Mach probe inside ATHENIS, front view.

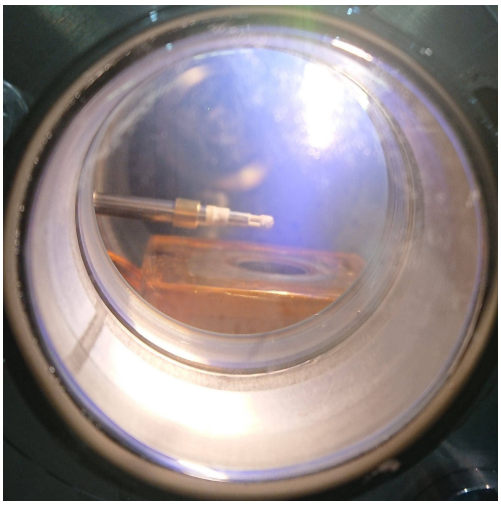

Figure 3.5: Mach probe inside ATHENIS, side view.

trode did not give any signal, so they were not analysed further. Probably, rotating the probe caused the contact between electrode and the wire to disconnect. After re-attaching all the contacts, two calibration curves were taken, at $V_{bias} = -70$ V represented in Figure 3.6, 3.7. The goal was to check for asymmetries and verify if the collecting areas of the four electrodes were the same, so the probe was rotated of 360° around its axis.

The graphs display the plot of current collected by each electrode versus time. It can be clearly seen that the North electrode behaves in a different way, as the shape of the curve has less pronounced peaks and is almost flat. Moreover, it could be easily noticed that the South electrode has a bigger average value with respect to others, and it also Has a greater slope in the ionic branch of the curve. This tendency is present in both the set of data collected: it could be assumed that the only two electrodes which can be used in the analysis are West and East, so the focus is moved on these two.

Other plots are presented (Figures 3.8, 3.10) in order to assess if there are significant changes of the average value between the two electrodes. It can be seen that there are some evident fluctuations in both of them, so it could be assumed that the system is not stable. Despite this fact, the analysis is carried out, using the information collected to calibrate results and to establish a method of analysis for future measurements.

The next step is to calculate the Mach number. It is defined as the ratio of the flow velocity to the ion sound speed[14], and it can be related to the ratio R of West (J_{west}) to East (J_{east}) ion saturation current densities[15]:

$$R = \frac{J_{west}}{J_{east}} = \exp(KM) \Longrightarrow M = \frac{1}{K} \ln\left(\frac{J_{west}}{J_{east}}\right)$$

If it is supposed, given the initial parameters of the system, that the plasma fits the kinetic, unmagnetized model ($K = 1$, Chung model in Table 3 of [15]), and assumed that the col-

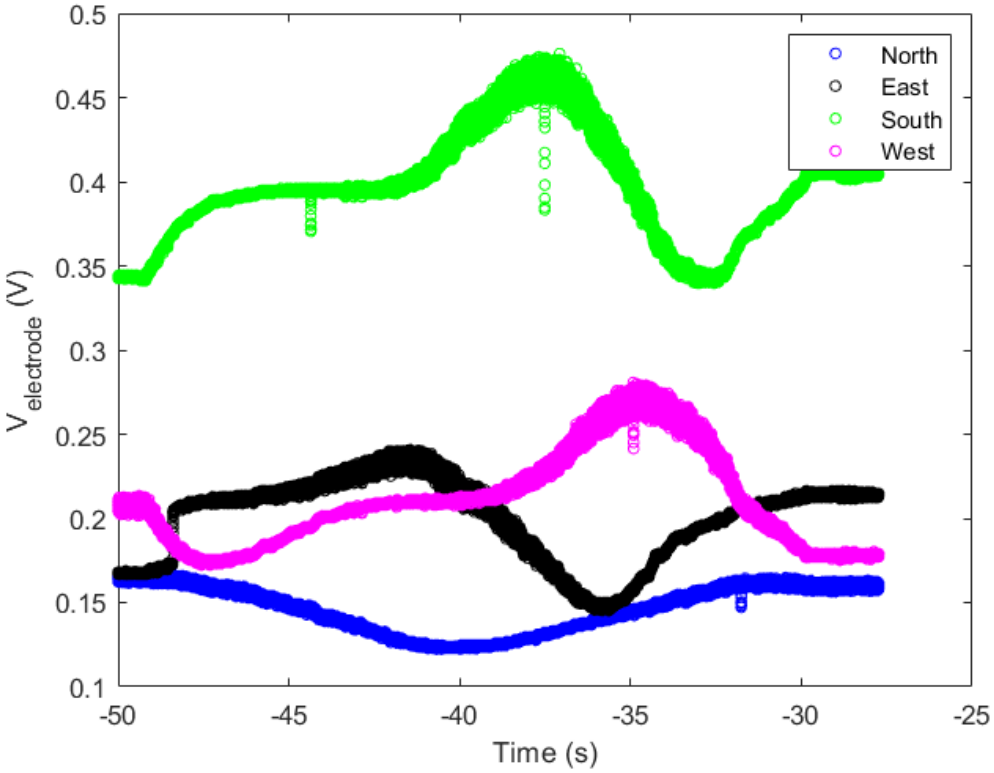

Figure 3.6: Voltages as a function of time during one full rotation of the probe around its axis, first sample.

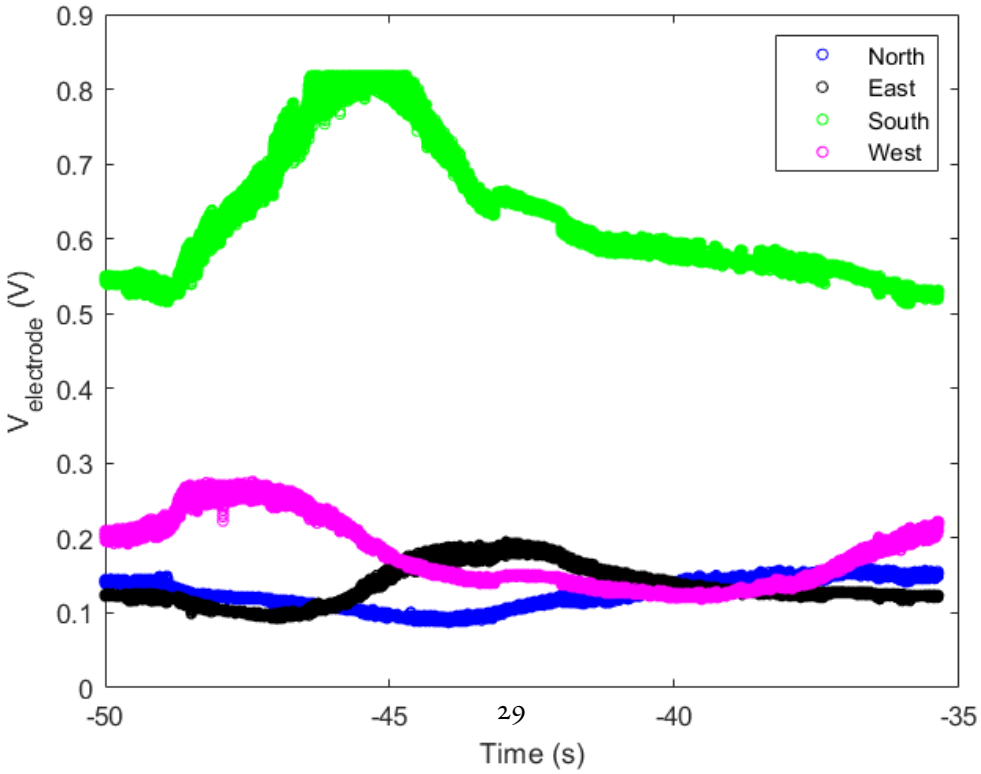

Figure 3.7: Voltages as a function of time during one full rotation of the probe around its axis, second sample.

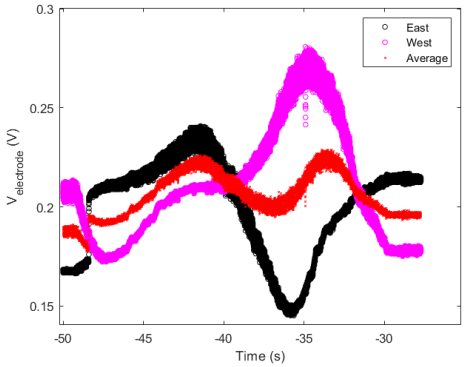

Figure 3.8: Voltages of E-W electrodes and their average as a function of time during one full rotation of the probe around its axis, first sample.

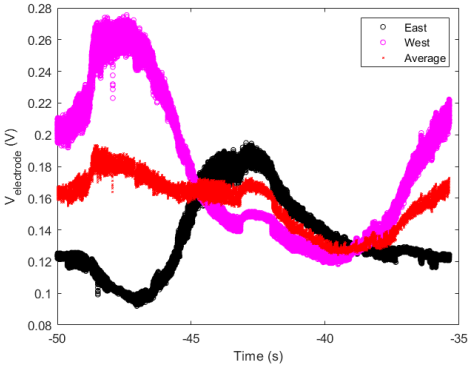

Figure 3.10: Voltages of E-W electrodes and their average as a function of time during one full rotation of the probe around its axis, second sample.

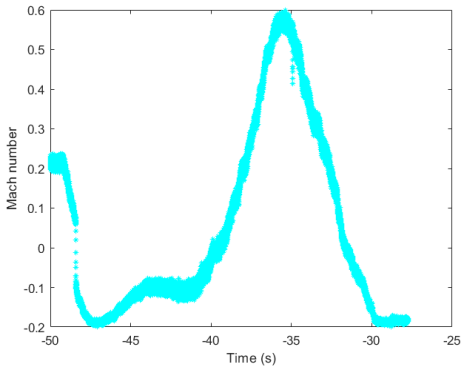

Figure 3.9: Mach number as a function of time, first sample.

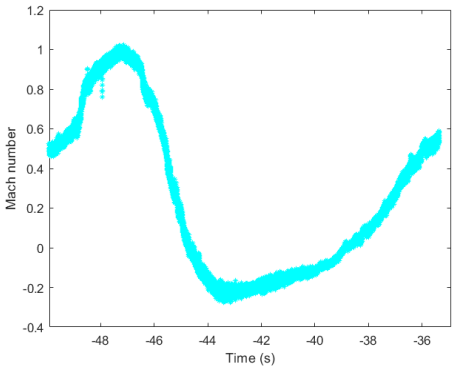

Figure 3.11: Mach number as a function of time, second sample.

lecting areas of the two electrodes are equal, the Mach number can be easily calculated as the natural logarithm of the ratio of West-East currents ($I_{electrode} = V_{electrode}/R_{shunt}$). A plot of how the Mach number changes through time (i.e. probe orientation) is shown in Figures 3.9 and 3.11.

One could observe that the Mach number's fluctuations are pretty relevant, as it changes in a range between 0.6 and -0.2 in the first set of data, and between 1 and -0.2 in the second one. However, the most important feature is that the plot of Mach number vs. time has roughly the same shape (maximums and minimums) when the probe has the same position

in plasma: indeed, the trend of all the graphs look similar but shifted. This may be a signal of the presence of a drift velocity in a particular direction, but it cannot be assured because of instabilities. Moreover, given the rough analysis of these graphs, it can be stated that the probe, while rotating, is not properly centred and moves by some millimetres, length that is comparable with the dimensions of the plasma. All this considered, East and West electrodes could be used for further measurements.

Angular analysis In order to properly estimate Mach number for different angular positioning of the probe and to correctly evaluate the incidence of plasma drift in the collected current, data needed to be analysed in ion saturation regime, so a bias tension of -60 V was chosen. At the beginning, only four main positions of the probe were considered: the current at $V_{bias} = -60$ V for East-West electrodes as a function of angular positioning is plotted in Figure 3.12. The currents were then normalised to the average current for each angles (Figure 3.13).

From 3.13 it could be seen that the West electrode collect about 30% more current than the East one. Besides, a validation of the hypothesis of eccentricity of the probe could be find if it is observed that current in S-E directions is greater for the West electrode: it might be that the probe moves in a more vivid plasma when it is in this orientation. Further analysis is conducted in the same way considering more angles; results are shown in Figures 3.14, 3.15.

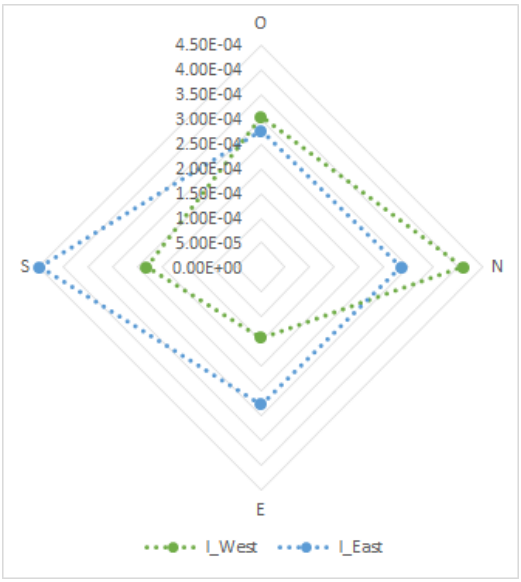

Figure 3.12: Angular diagram (4 angles), E-W current at $V_{bias} = -60$ V.

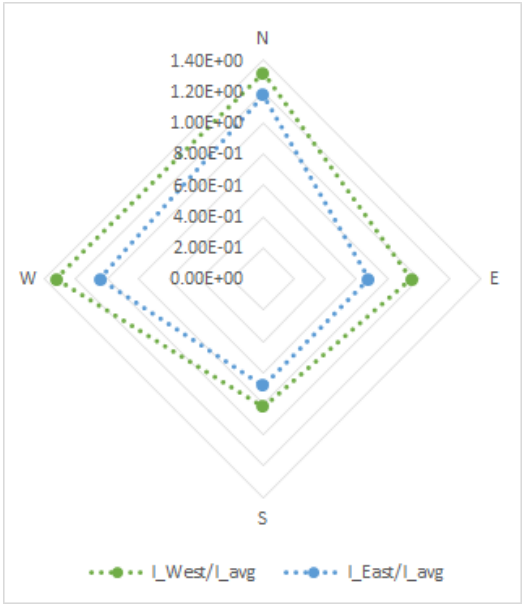

Figure 3.13: Angular diagram (4 angles), E-W current at $V_{bias} = -60$ V, normalised to the average current.

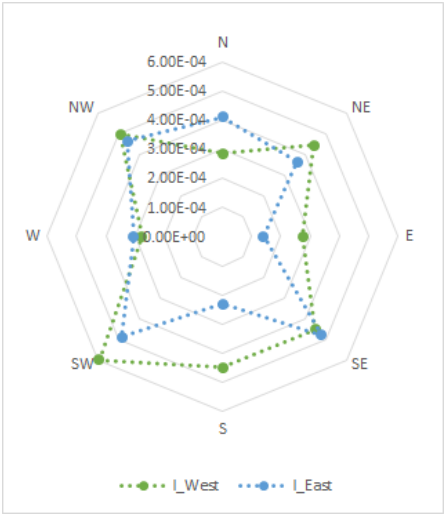

Figure 3.14: Angular diagram (8 angles), E-W current at $V_{bias} = -60$ V.

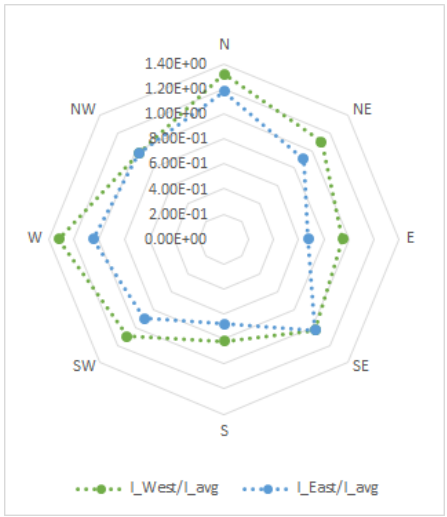

Figure 3.15: Angular diagram (8 angles), E-W current at $V_{bias} = -60$ V, normalised to the average current.

For the "45°" measures, plasma is different (and likely stronger) than before, as these measures were taken after some time. Figure 3.16 suggests in any case that current in S-E, S-W direction is greater. Moreover, electrode West collects more current than the East one even in these samples (3.15).

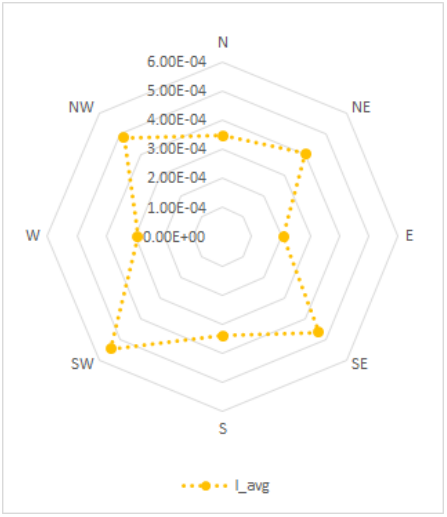

Figure 3.16: Angular diagram (8 angles), average current collected by E-W electrodes at $V_{bias} = -60$ V.

ION SATURATION CURRENT To proceed with more precise analysis, a MATLAB program was used to calculate ion saturation current for E-W electrodes in each position studied: a linear fit in the saturation regime of the I-V curve was made with fit function $I = p_1 \cdot V + p_2$; $I_{saturation}$ was estimated as the ordinate of the fitted line when $V = V_{float}$, with V_{float} floating potential obtained from the program. The results are shown in Table 3.1, while some explanatory graphs display how the fit was done (Figures 3.17, 3.18, 3.19).

All the fits could be considered good as both sse and rmse are very close to zero* and data are not scattered but follow a line properly.

Ion saturation current is confirmed to be about 30% more for West electrode even with this more precise data. A correction factor of 1.3 is therefore used to calibrate the West electrode: Mach number is calculated again ($\mathcal{M}_{corrected} = \ln(\frac{I_{sat,W}}{1.3 \cdot I_{sat,E}})$) and compared with the one without correction ($\mathcal{M} = \ln(\frac{I_{sat,W}}{I_{sat,E}})$), results are shown in Figure 3.20.

The two significant directions are N-S and W-E, because, as it could be seen in 3.21, E-cross-

*https://it.mathworks.com/help/curvefit/evaluating-goodness-of-fit.html

	$p_1(\cdot 10^{-6}\frac{A}{V})$	$p_2(\cdot 10^{-4}A)$	sse	dfe	rmse $\cdot 10^{-6}$	$I_{sat}(\cdot 10^{-4}A)$
W_W	-1.3169	1.8655	7.2911E-07	1.2431E+05	2.4219	1.6886
W_E	-0.7851	0.8899	3.8959E-07	1.2431E+05	1.7703	0.7840
N_W	-1.1980	2.1038	9.4157E-07	8.6465E+04	3.2999	1.9443
N_E	-1.2492	1.4969	8.6181E-08	8.6465E+04	0.9984	1.3306
E_W	-1.4733	1.8727	1.2546E-06	1.7952E+05	2.6435	1.6506
E_E	-1.6295	2.0568	2.3828E-06	1.7952E+05	3.6432	1.8112
S_W	-2.1678	3.1752	1.9229E-06	1.7097E+05	3.3536	2.8372
S_E	-2.1273	2.8269	4.1370E-06	1.7097E+05	4.9190	2.4953
SW_W	-2.9894	4.1918	1.1782E-06	3.5239E+04	5.7823	3.6898
SW_E	-2.2231	2.2452	8.7045E-08	3.5239E+04	1.5717	1.8719
SE_W	-2.5324	3.0325	6.7137E-07	2.8889E+04	4.8207	2.6113
SE_E	-2.7167	3.0517	2.7454E-07	2.8889E+04	3.0827	2.5999
NW_W	-2.5130	3.4378	1.1902E-06	9.1051E+04	3.6155	3.0027
NW_E	-2.6374	3.1784	4.3662E-06	9.1051E+04	6.9248	2.7218
NE_W	-2.3754	2.9573	1.8444E-06	1.0844E+05	4.1241	2.5632
NE_E	-2.7347	3.2406	1.7730E-06	1.0844E+05	4.0435	2.7868

Table 3.1: Fit and goodness of fit parameters for each position of the probe. In particular: sse stands for Sum of Squares Due to Error and evaluates the total deviation of the response values from the fit to the response values; dfe is the number of degree of freedom; rmse means Root Mean Squared Error. The first column refers to which position and which electrode is considered, referred as $Position_{Electrode}$

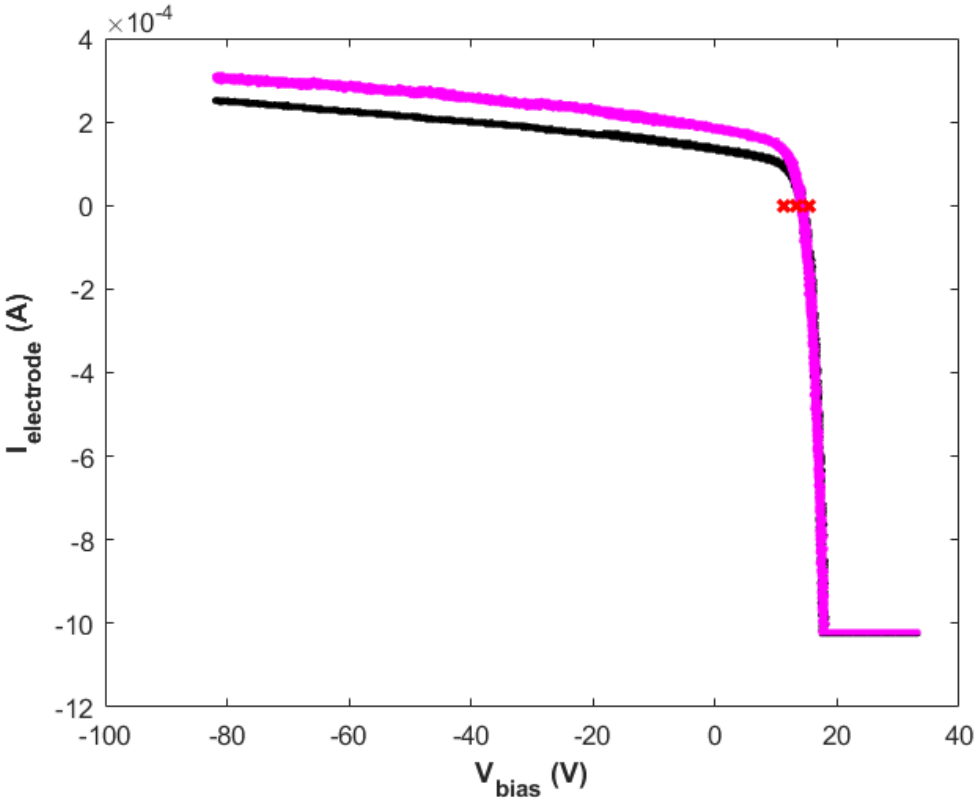

Figure 3.17: Current-voltage characteristic curve for N-orientated West electrode set of data. In pink the current collected by W, in black the one collected by E.

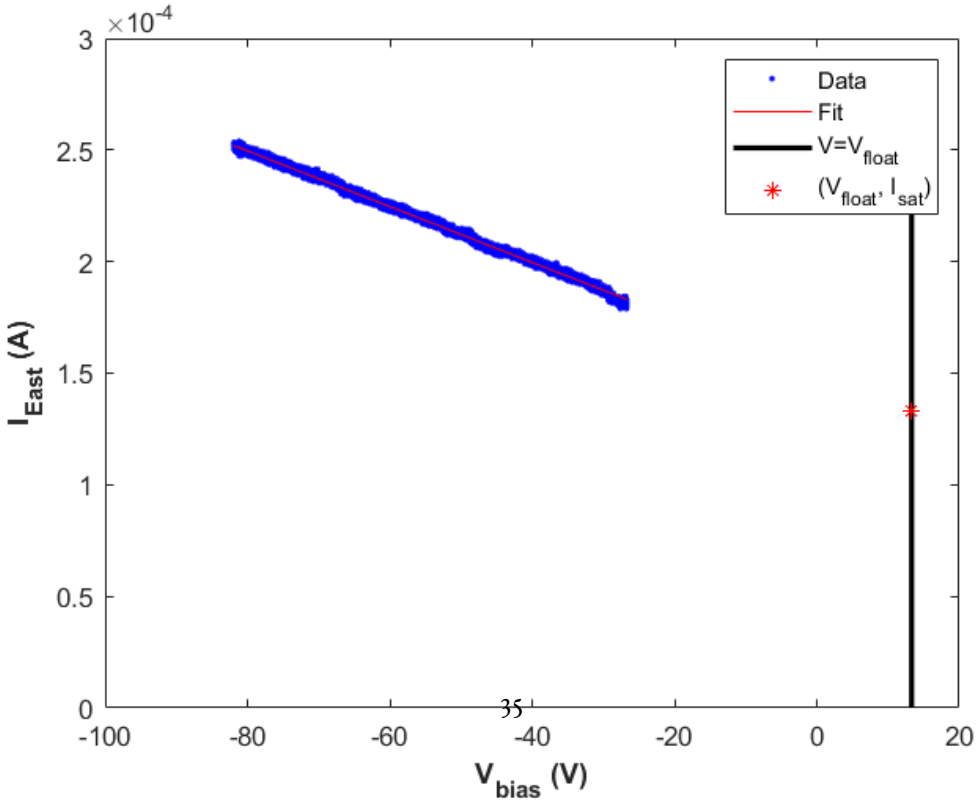

Figure 3.18: Data chosen for the fit, fitted line and representation of the floating potential, East electrode.

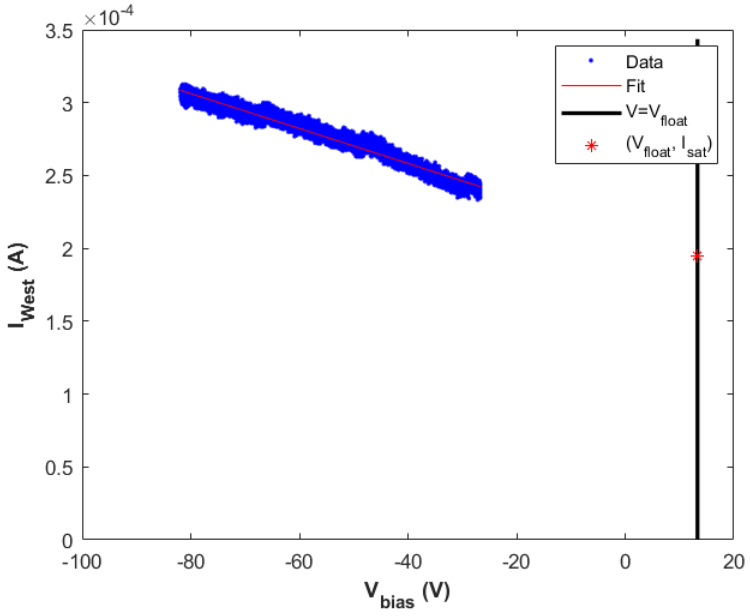

Figure 3.19: Data chosen for the fit, fitted line and representation of the floating potential, West electrode.

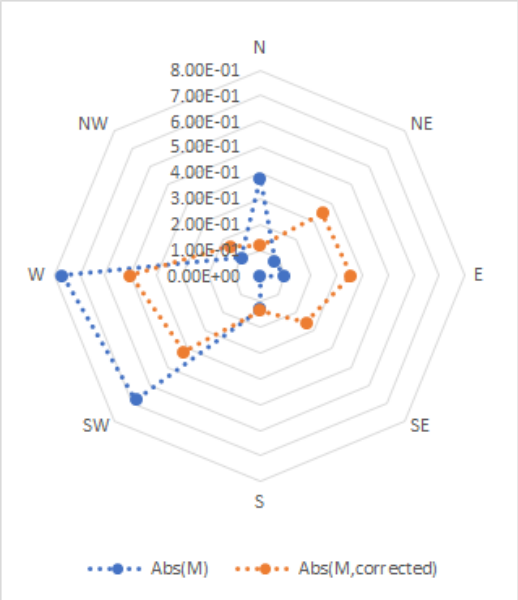

Figure 3.20: Angular plot of the Mach number with corrections.

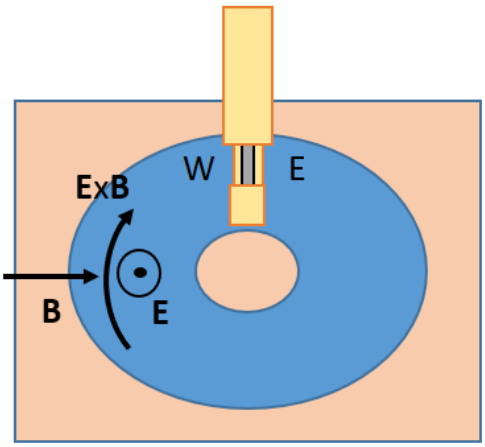

Figure 3.21: Orientation of the probe in the plasma.

B drift velocity is expected to be in W-E direction, while the azimuthal velocity along with N-S axis.

It is finally obtained, by averaging West-East, North-South corrected Mach numbers:

$$\mathcal{M}_{\vec{E}\times\vec{B}} \approx 0.43$$

$$\mathcal{M}_{azimuthal} \approx 0.13$$

Conclusion These problems were identified during the experiment and the analysis:

- the probe resulted not to be properly centred: while rotating, it moved about 1 mm, which might be the length of plasma channel: this could be a reason for the spiked and asymmetrical shape of the angular diagrams.
- the collecting area of the electrodes was not likely the same: it could be the South electrode was more exposed to the plasma then the others, given that it was more radially protruding. Probably also the correcting factor which was considered for West electrode analysis was due to its bigger collecting area, but it cannot be assured.
- After the first measurements, the North electrode disconnected, so it cannot be assured that contacts also of the other electrodes were perfectly isolated and welded.

The various construction imperfections and the variability in the experimental conditions causes the probe not to be appropriate for further analysis. A new project was therefore made in order to estimate plasma parameters.

3.2 The new probe

New probe project Two main adjustments were made in order to avoid the previously mentioned problems:

- a new rotation system, with a more precise manipulator and a steadier central axis, was used (Figure 3.22). The wires were better shielded and tided to the support, their tinning was also made with more attention. Moreover, the angle-measuring system improved with the new manipulator. Finally, the vacuum isolation was carefully checked and improved, but the connection system remained the same of the old probe.

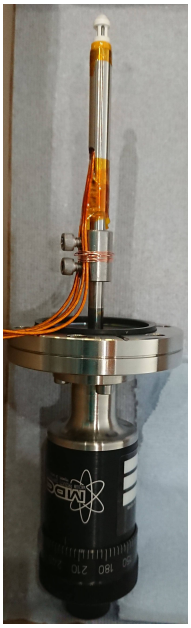

Figure 3.22: New rotating system, assembled with the new probe.

Figure 3.23: New probe tip, with Boron Nitride support and ceramic glue.

- a new support made of Boron Nitride was prepared, in order to have equal collecting areas on the four electrodes. Details on dimensions are specified in Figure 3.24. The probe tip was protected by ceramic glue and better welded to the rotating system (Figure 3.23).

Figures 3.25 and 3.26 are actual pictures of the installation of the probe inside ATHENIS.

Analysis The new probe proved to work much better than the old one: in fact the shape of the voltage measured in time is roughly the same, like average values, which vary in a small range.

It could be observed that South and East electrodes collected more current than West and North ones: it may be that the collecting areas are not exactly the same, but differently than before the difference is less important ($\approx$ 20%). As a consequence, currents collected by these two electrodes will be corrected considering this side effect. An interesting feature is observed if opposite electrodes are coupled: it could be clearly seen that the differences evened

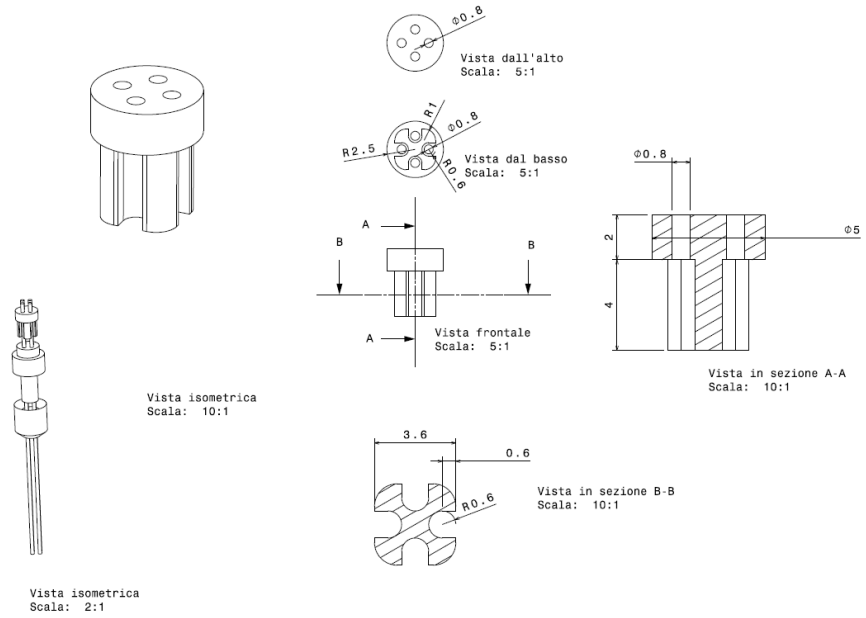

Figure 3.24: Project of the Boron Nitride support.

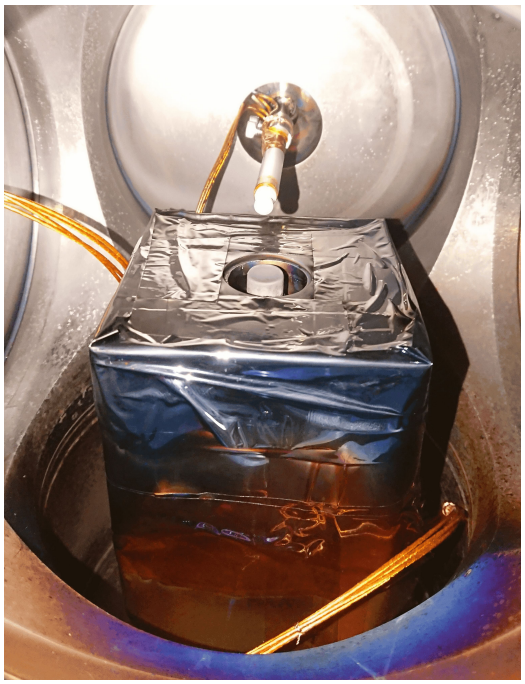

Figure 3.25: New probe inside ATHENIS, front view.

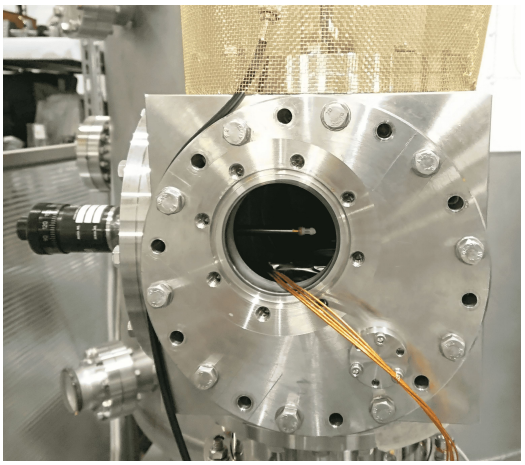

Figure 3.26: New probe inside ATHENIS, side view.

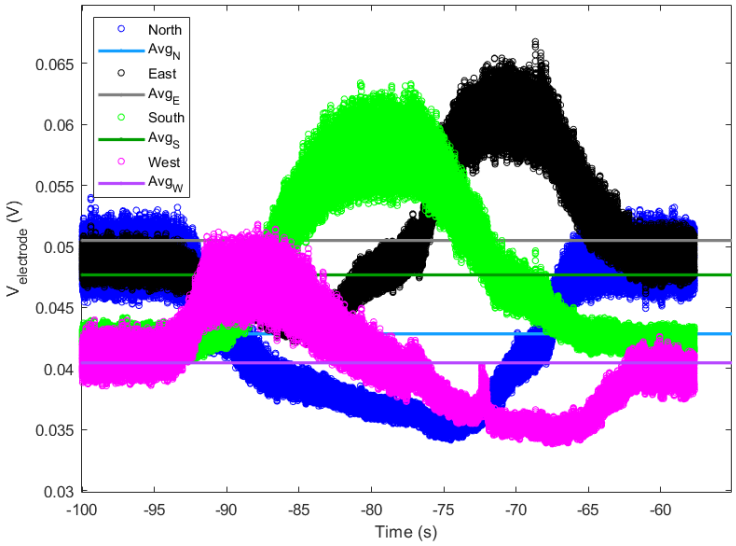

Figure 3.27: Voltages vs. time for each electrode during one full clockwise rotation of the new probe.

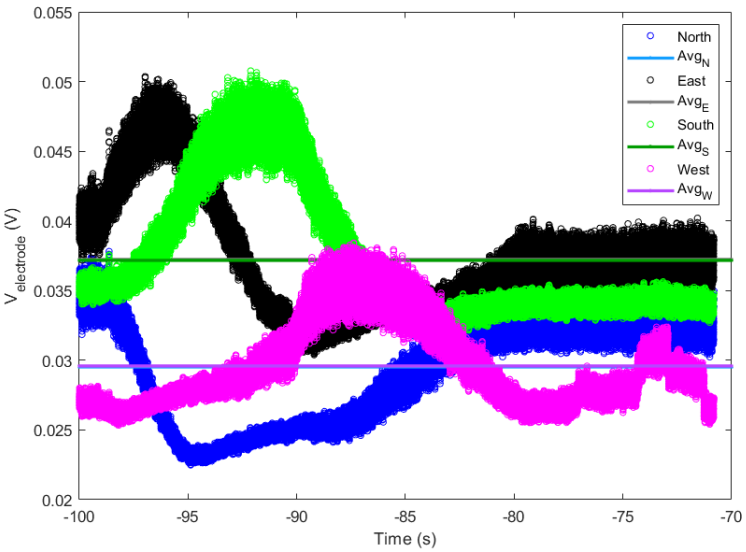

Figure 3.28: Voltages vs. time for each electrode during one full anti-clockwise rotation of the new probe.

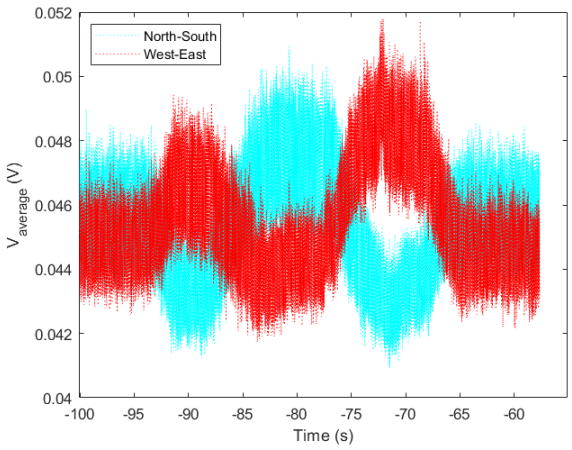

Figure 3.29: Voltages vs. time for each electrode during one full clockwise rotation of the new probe.

out and that the shape of the voltage-time curve is symmetrical (Figures 3.29 and 3.30).

So it can be assumed that the probe is working properly. The analysis was then conducted with two different methods: the linear fitting of the ion saturation, just like in Paragraph 3.1, where ion saturation current $I_{sat,0}$ and plasma density $n_0 = \frac{I_{sat,0}}{0.6 \cdot A \cdot e \cdot c_{s0}}$[†] are obtained, and the 4 parameter fit[16]. The fitting curve is the following one:

$$I = 0.6 \cdot e \cdot A \sqrt{\frac{eT_e}{m_i}} \cdot n[1 + R(V_f - V)] \left[1 - \exp\left(e\frac{V - V_f}{kT_e}\right)\right]$$

where the fitting parameters are:

- n: plasma density;
- T_e: electron temperature;
- R: parameter for correction on the ion saturation;
- V_f: floating potential.

all obtained using MATLAB with a non-linear fitting method.

[†]where A is the collecting area, e is the electron charge, c_{s0} the ion sound speed with estimated electron temperature of 5 eV and factor 0.6 is for considering the pre-sheath approximation([14], (3.2.20) formula).

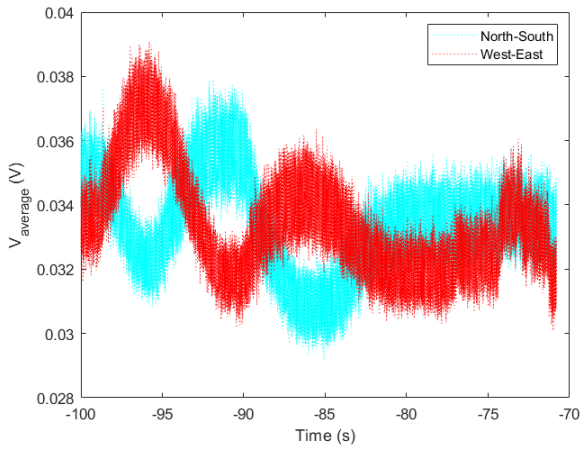

Figure 3.30: Voltages vs. time for each electrode during one full anti-clockwise rotation of the new probe.

From n and T_e, ion sound speed $c_s = \sqrt{\frac{eT_e}{m_i}}$ and then ion saturation current $I_{sat} = 0.6 \cdot e \cdot \mathcal{A} \cdot n \cdot c_s$ are calculated.

Four sets of data were collected and analysed, each one with a different orientation of the probe (North electrode facing the four main cardinal points).

In the next figures some explanatory graphs are shown (3.31, 3.32, 3.33), while results are presented in Table 3.2.

It can be observed that plasma densities and saturation currents have the same order of magnitude in both fit models, but in the most rough one are a bit overestimated. They are in any case comparable and that is a prove of consistency.

An estimate of plasma density and electron temperature can therefore be provided:

$$n = 2.6 \cdot 10^{15} \mathrm{m}^{-3}$$

$$T_e = 4.6\,\mathrm{eV}$$

The next step is to evaluate Mach number and drift velocity.

By using the parameters derived from the fit and the fitting function, current at $V =$

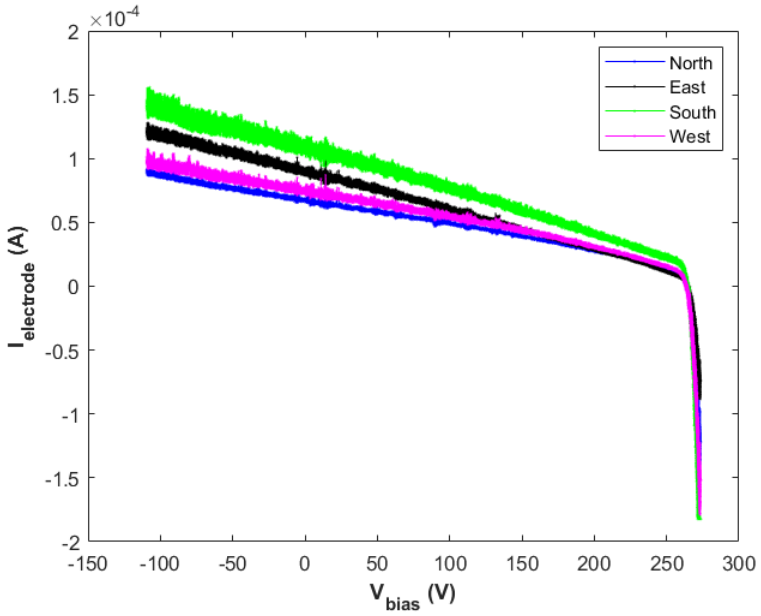

Figure 3.31: Characteristic curve for all the 4 electrodes while electrode North is facing up.

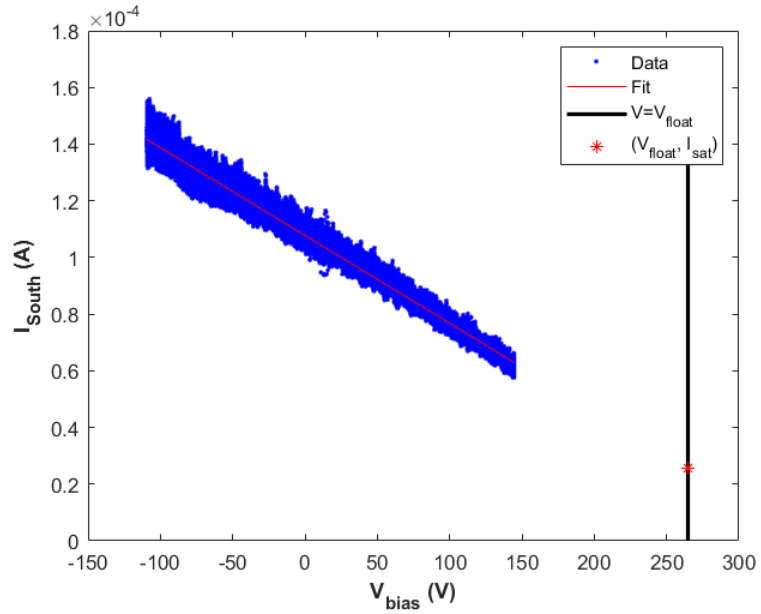

Figure 3.32: Data chosen for the fit, fitted line and representation of the floating potential, South electrode facing down.

	$I_{sat,0}(\cdot 10^{-5}\mathrm{A})$	$n_0(\cdot 10^{15}\mathrm{m}^{-3})$	$n(\cdot 10^{15}\mathrm{m}^{-3})$	$T_e(\mathrm{eV})$	$R(\mathrm{V}^{-1})$	$V_f(\mathrm{V})$	$I_{sat}(\cdot 10^{-5}\mathrm{A})$
W	2.0852	3.32327	2.6325	4.2627	0.014842	265.24	1.5251
E	0.8075	1.28695	1.6525	3.8647	0.025831	263.05	0.9116
N	2.9493	4.70042	3.7166	3.9909	0.01434	265.12	2.0834
S	3.2190	5.13025	4.3174	3.9126	0.010212	264.03	2.3964
W	2.2456	3.57890	2.8704	4.3918	0.010519	262.91	1.6880
E	1.0364	1.65175	2.2747	3.9861	0.023388	262.87	1.2744
N	1.9824	3.15943	2.1973	4.8289	0.016713	263.41	1.3549
S	2.1996	3.50559	2.8991	4.0777	0.015655	261.37	1.6427
W	2.0247	3.22685	2.6956	4.5898	0.01356	262.58	1.6205
E	1.2185	1.94197	1.4611	6.189	0.029424	261.85	1.0110
N	1.7084	2.72275	2.2989	4.5842	0.014724	262.9	1.3811
S	2.4858	3.96172	3.5728	4.4434	0.015393	263.15	2.1133
W	2.3832	3.79820	3.1421	4.9988	0.013339	262.69	1.9713
E	1.4964	2.38487	1.9265	5.4948	0.020428	261.55	1.2672
N	1.4872	2.37021	1.9996	5.3956	0.015922	261.08	1.3034
S	1.7834	2.84228	2.4717	4.8084	0.018114	262.09	1.5209

Table 3.2: Fit parameters for each position of the new probe. Different sets of data (i.e. each probe angular inclination) are separated by a line, the letter points out which electrode is considered.

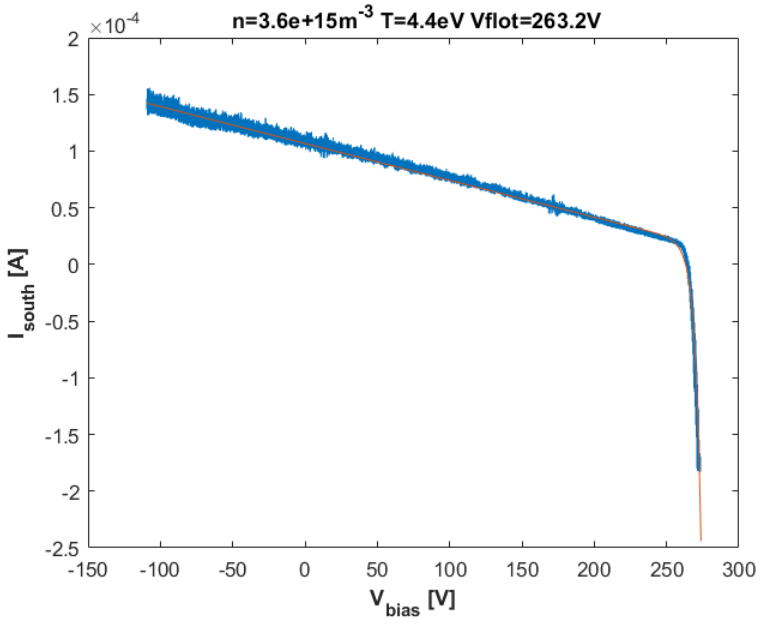

Figure 3.33: Characteristic curve I vs. V for South electrode facing down and fitting 4-parameters curve.

−100 V is calculated: this current is mainly due to ion movements and it is in full saturation regime, so it is the most relevant to analyse.

The two axes of interest are, just like the previous section, the North-South (for azimuthal drift velocity) and West-East ($\vec{E} \times \vec{B}$ drift velocity). Mach number is calculated for each configuration of the probe as the natural logarithm of the ratio of currents collected, after correcting the offset pointed out in Figures 3.27 and 3.28 (i.e. the 20% more of current collected by South and East electrodes). Respectively, $\mathcal{M}_{az} = \ln\left(\frac{I_\downarrow}{I_\uparrow}\right)$ and $\mathcal{M}_{\vec{E}\times\vec{B}} = \ln\left(\frac{I_\rightarrow}{I_\leftarrow}\right)$, where subscripts refers to position of the electrode in a particular sample. After that, drift velocity in each direction is calculated as $v_d = c_s \cdot \mathcal{M}$ [15]. Results are presented in Tables 3.3 for azimuthal direction and 3.4 for $\vec{E} \times \vec{B}$.

The estimated values are comparable with each other but with some outliers, which can be due to changes in the plasma, experimental issues or other systematic errors: proper average values cannot be calculated, so the analysis is limited to a coarse but reasonable evaluation,

$I_{\downarrow}$ (A)	$I_{\uparrow}$ (A)	$I_{\downarrow}/I_{\uparrow}$	$\mathcal{M}$	$c_s(\mathrm{m\,s^{-1}})$	$v_d(\mathrm{m\,s^{-1}})$
1.29919E-04	1.13048E-04	1.4365	0.362243433	4595.208777	1664.584201
1.20897E-04	8.13165E-05	1.1894	0.173447234	4852.959615	841.7324241
1.39267E-04	8.76128E-05	1.2717	0.240320528	4911.132744	1180.246014
1.15082E-04	1.06263E-04	1.3537	0.302869726	5294.900114	1603.664944

Table 3.3: Currents collected in direction $\uparrow, \downarrow$, azimuthal Mach number and drift velocity estimates.

$I_{\rightarrow}$ (A)	$I_{\leftarrow}$ (A)	$I_{\rightarrow}/I_{\leftarrow}$	$\mathcal{M}$	$c_s(\mathrm{m\,s^{-1}})$	$v_d(\mathrm{m\,s^{-1}})$
9.79273E-05	9.46037E-05	1.2939	0.257671799	4659.843554	1200.710269
9.58420E-05	1.09361E-04	1.0955	0.091188878	4878.10892	444.8292801
1.18797E-04	9.58784E-05	0.9912	0.008810619	5366.371393	47.28105336
1.14961E-04	8.79645E-05	1.0455	0.044519701	5221.325208	232.4518373

Table 3.4: Currents collected in direction $\rightarrow, \leftarrow, \vec{E} \times \vec{B}$ Mach number and drift velocity estimates.

which gives:

$$\mathcal{M}_{\vec{E}\times\vec{B}} \approx 0$$

$$v_{d,\vec{E}\times\vec{B}} = 480\,\mathrm{ms^{-1}} \ll 0.1 c_s$$

$$\mathcal{M}_{azimuthal} = 0.3$$

$$v_{d,azimuthal} = 1300\,\mathrm{ms^{-1}}$$

So it can be concluded that there is a plasma drift along N-S direction detected from the fluxes of positive ions, while it is almost absent in the other direction.

This is consistent with the concept of Hall-thrusters, according to which positive ions are accelerated along the azimuthal direction by the electric field (to realise thrust) while electrons are confined in the $\vec{E} \times \vec{B}$ drift (to sustain the ionization process).

Final observations After all the measurements were taken, the probe was extracted from ATHENIS and resulted quite ruined (Figure 3.34): as a matter of facts, the Argon plasma sputtered significantly on the probe, this could result in a change in the collecting area and generally on the effectiveness of the probe. This effect should be limited in SPIDER as the plasma is made of Hydrogen, which is less aggressive on the surface of the probe.

Figure 3.34: Sputtered probe after the measures.

3.3 Conclusions

In conclusion, a workable design of the probe was obtained, at least in the second iteration. In order to use it on ATHENIS:

1. the probe needs to be correctly centred and it needs to be able to rotate freely;
2. the manipulating system needs to be precise enough to guarantee appropriate orientation of the probe inside the experiment;
3. connection and vacuum isolation are required to be adequate;
4. a full rotation of the probe is demanded in order to calibrate collecting areas of the electrodes;

However, the probe cannot be rotated in SPIDER. For the next experimental campaign, it is suggested to use the calibration that was found in ATHENIS, which showed that South and East electrodes collect about 20% more current with respect to the others.

The world ends with you. If you want to enjoy life, expand your world. You gotta push your horizons out as far as they'll go.

Sanae Hanekoma

4

ADEL probe - A Double Electrode Langmuir probe

Another type of probe was analysed: a double Langmuir probe. It is of interest because it would consist in a totally floating measuring system; besides, testing this kind of probe in a RF source would help understand if it is suitable for measurement on SPIDER. A collaboration with the experiment CRISP (Compact RF Ion Source Prototype for emittance scanner testing) permitted to do this. The goal was giving an estimate of the two main plasma parameters: electron temperature T_e and plasma electron density n_e.

Figure 4.1: ADEL assembled.

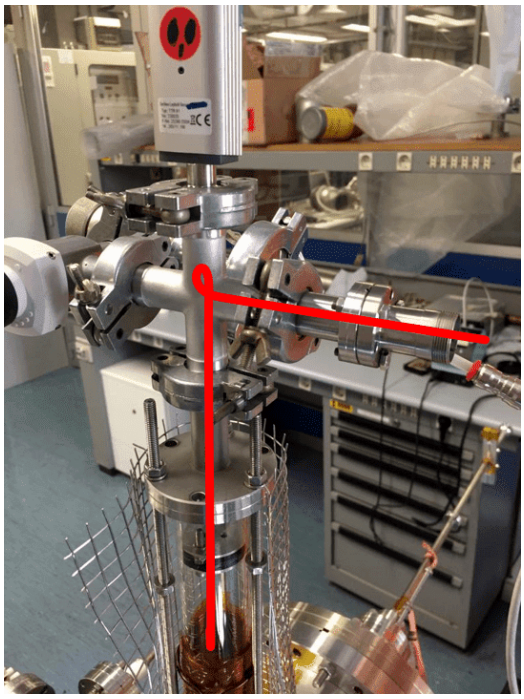

Figure 4.2: Scheme of ADEL positioning inside CRISPy.

4.1 The probe and the experimental set-up

The probe (Figure 4.1) consists of two filaments made of tungsten, whose diameter is 0.25 mm and height is 6 mm, isolated with high-temperature compatible and plasma-compatible insulation materials (i.e. alumina Al_2O_3 ceramic beads and alumina glue). The two electrodes are 2.6 mm apart and parallel (the angle between the wires was corrected after the picture in Figure 4.1 was taken). The probe is inserted inside the plasma chamber of CRISPy as shown in Figure 4.2, 4.3, 4.4.

The electronic acquisition system (Figure 4.5) is composed of a shunt resistance, that could be changed according to the collected current, connected in series to a voltage regulator circuit. That circuit could control the output voltage within the range 0-36 V approximately, it is based on four 9 V batteries and it is represented as *Vfix* in Figure 4.6. A variable num-

Figure 4.3: CRISPy plasma chamber.

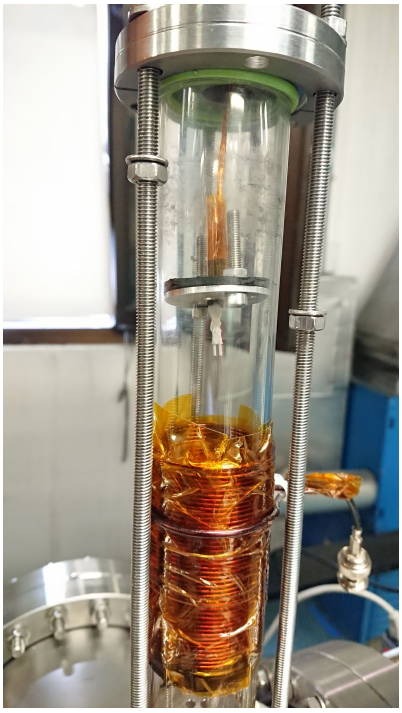

Figure 4.4: ADEL positioning inside CRISPy.

ber of other batteries can be added in series in order to move (as an offset) the range of data acquired. The shunt resistance used is $Rshunt = 1105(11)\ \Omega$.

Measurements were taken in two different methods. The first sets were collected using multimeters, to measure *Vbias* and *Vshunt*, and recorded manually. The second sets, instead, were collected with a DL716 Yokogawa 16 channels digital scope, with a 50 kHz filter on both channel used and an acquisition rate of 10 kilosample per second.

For more details on the source and CRISPy experiment, see [17].

4.2 Analysis

Model used

Let the following expressions be:

- $\alpha = I_{sat,A}/I_{sat,B}$ ratio between saturation current of the two probe electrodes;
- $V := V_B - V_A$;

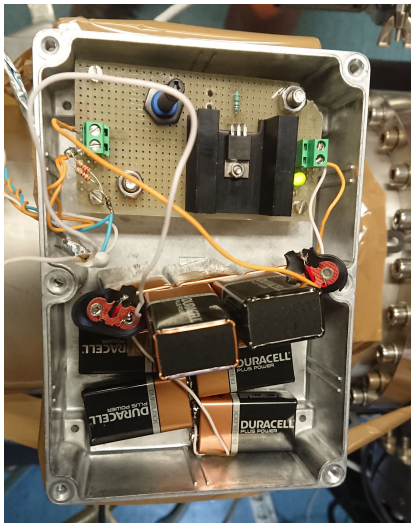

Figure 4.5: Metal box with electronic components of the acquisition system.

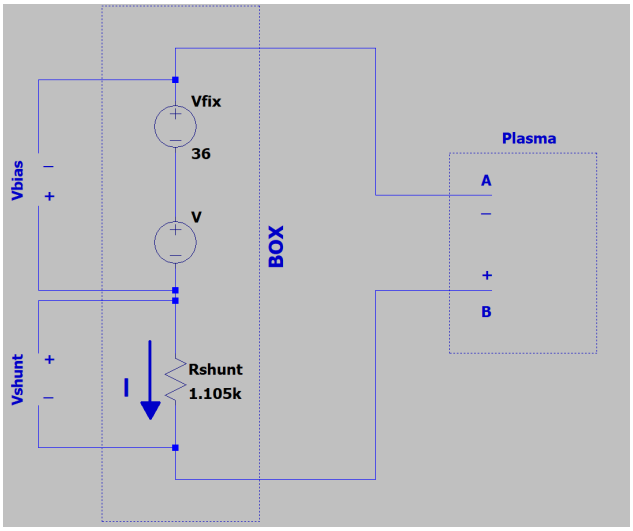

Figure 4.6: Circuit scheme of the acquisition system.

- $V_f := V_{fB} - V_{fA}$ difference between the two floating potentials;

It could be hypothesize, according to [5], that:

$$I_A + I_B = 0$$

$$I_{A,B} = I_{satA,B}\left(1 - \exp\left(\frac{e(V_{A,B} - V_{fA,B})}{k_B T_e}\right)\right)$$

After some calculations, it could be obtained that:

$$I(V) = \alpha I_{sat,A} \cdot \frac{\exp\left(\frac{V-V_f}{k_B T_e}\right) - 1}{\alpha \exp\left(\frac{V-V_f}{k_B T_e}\right) + 1}$$

and, if $\alpha = 1$, id est the two electrodes are identical:

$$I = I_{sat,A} \tanh\left(\frac{V - V_f}{k_B T_e}\right)$$

As a consequence, the $I - V$ curve should be symmetrical with respect to the origin of the

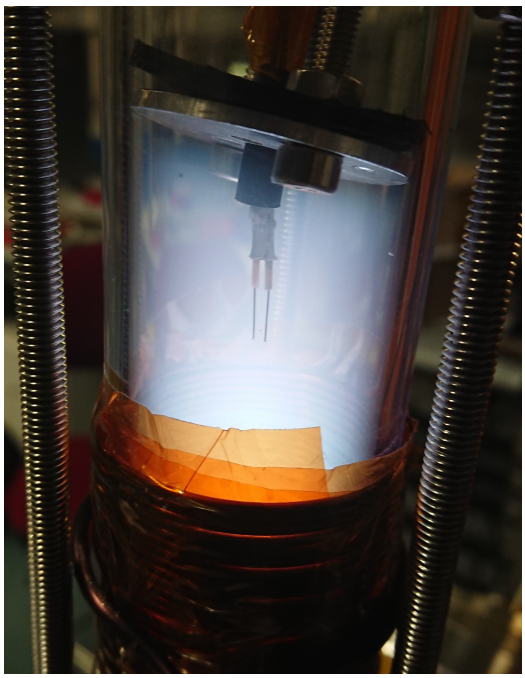

Figure 4.7: ADEL in helium plasma.

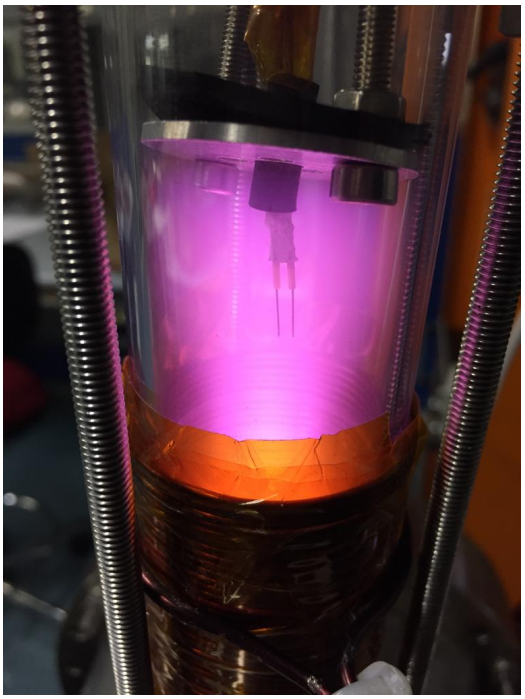

Figure 4.8: ADEL in air plasma.

axis.

The approximation with $\alpha = 1$ was not used to fit data because one could not be sure of the perfect symmetry of the probe, hence of the characteristic I-V curve.

Analysis Data were collected with two different RF frequencies (13 MHz and 72 MHz), corresponding to the two main resonances, where the plasma generated is brighter. Plasma was made with low pressure helium or air (pressure in the vessel was kept always around $\approx$ 20 Pa). Some pictures of the probe in the plasma can be found in 4.7 and 4.8.

For each set of data, the potentiometer was used to change the bias potential, and voltage across the shunt resistance is registered.

As previously stated, measures were collected in two ways: by manually taking couples of ($Vbias$, $Vshunt$) using two multimeters, or by using a digital scope.

Gas	M/D	f(MHz)	$n(\cdot 10^{16}\mathrm{m}^{-3})$	T_e(eV)	$R(\mathrm{V}^{-1})$	V_f(V)	α
Air	M	13	4.4716	6.8496	0.0083438	-0.10985	0.93069
Air	D	13	4.1305	6.5303	0.0028294	2.4439	1.2461
He	M	13	2.7688	14.476	0.0010711	-0.22008	0.84512
He	D	13	1.5521	11.284	0.011001	8.0448	1.2525
He	M	72	1.9379	9.2694	0.009260	0.47409	0.87957
He	D	72	1.7868	9.879	0.0094407	5.7351	0.84636
Air	M	72	8.1875	2.6512	0.037926	1.0552	0.91902

Table 4.1: Fit results. Notation: M stands for Manual acquisition, D for Digital scope. The Digital sample at 13 MHz for air is absent because plasma was highly unstable, to the point that measurements were impossible.

In both cases, a MATLAB program was used to fit data with the following fitting expression:

$$I(V) = 0.6 \cdot n \cdot \sqrt{\frac{eT_e}{m_i}} \cdot \mathcal{A}_{coll} \cdot e \cdot (1 + R|V_f - V|) \cdot \alpha \cdot \frac{\exp(V - V_f)/T_e - 1}{\alpha \exp(V - V_f)/T_e) + 1}$$

where R is a parameter used to take into account the slope of ionic saturation branch of the curve, n is the plasma density, m_i is the ionic mass (which could be $m_{Air} = 4.83632 \cdot 10^{-26}$kg or $m_{He} = 6.68 \cdot 10^{-27}$kg) and $\mathcal{A}_{coll} = 4.3354 \cdot 10^{-6}\mathrm{m}^2$ is the collecting area of the electrode.

Results of the fit are reported in Table 4.1, an explanatory graph is in Figure 4.9.

Observations As far as it is known, in each configuration the plasma could be very different. Nevertheless, the two plasma parameters of our interest (T_e and n) seem to be contained in a limited range of values.

By comparing samples taken with the same plasma conditions, but with different approaches (manual or digital), it could be observed that parameters are very close to each other: the probe behave in the same way for the same setting.

It could be interesting to observe that the model with the $\alpha = 1$ approximation would not

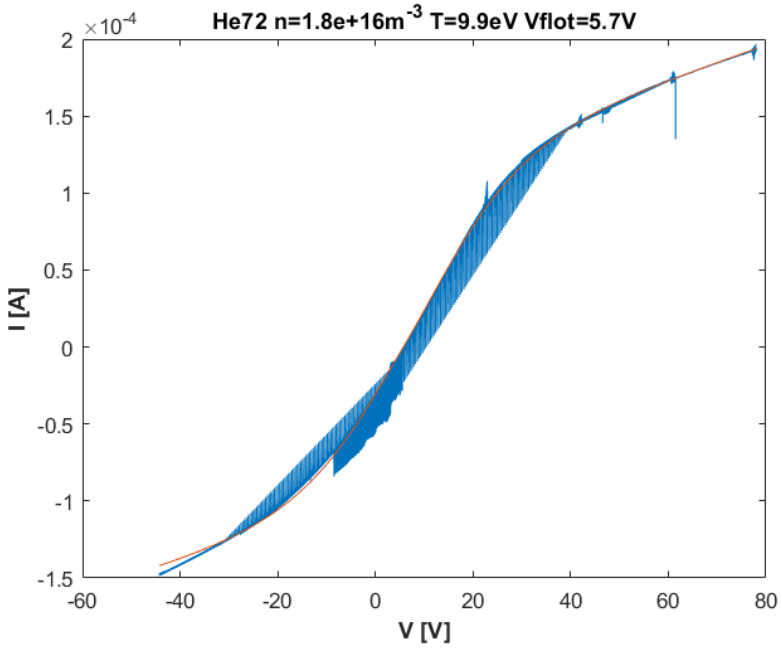

Figure 4.9: $I - V$ curve and fitted function for ADEL in helium plasma, RF frequency 72 MHz

have fitted the data adequately: in fact, α varies in a range between 0.85 and 1.25, this is a clear sign of the slight difference of the current collection between the two electrodes of the probe: this could be due to a small geometrical asymmetry of the two electrodes, but more probably, it is due to the probe position inside the small plasma volume. The spacing between the electrodes is about one tenth of the diameter of the plasma column; therefore, a small positioning error with respect to the axis of the plasma chamber could cause the probe to see radial plasma gradients and therefore asymmetry of the collected current to each electrode.

4.3 Conclusions

In conclusion, it can be stated that the probe works properly but is sensitive to sudden tension shifts. The previously stated theory fitted properly the data, so that electron temperature and plasma density could be estimated.

The plasma in CRISP is not a particularly cold plasma ($T_e \approx 10$eV) but could reach a good density ($n \approx 3 \cdot 10^{16}$), enough for fulfilling its purpose.

Concerning the use in SPIDER, it is worth noticing that under certain conditions, the fit of the current-voltage characteristics could provide a relatively low electron temperature (see 7th measurement in Table 4.1). It is also worth noticing that a reduced current unbalancing among the electrodes is to be expected, as the plasma non-uniformities should be minimal on the scale of the probe dimension.

Science, almost from its beginnings, has been truly international in character. National prejudices disappear completely in the scientist's search for truth.

Irving Langmuir

5

Langmuir probes

The Langmuir probe is the last type of probe analysed. The main issue with the present Langmuir probe design is that it cannot be tested in a RF plasma, similar to the the SPIDER source plasma and so its correct behaviour cannot be confirmed. On the other hand, testing the probe in an even slightly different system would not provide certainty as to the compensation method, so that a numerical analysis was considered more sensible and effective.

5.1 Statement of the problem

The use of Langmuir probes in DC plasmas is now well established. However, in RF plasmas the RF component across the probe sheath distorts the I–V curve and shifts it, making

it more negative, so that DC theory cannot be used directly ([18]). This mainly happens because plasma potential V_p could be oscillating with an average value V_{p0} due to radio-frequency component $\tilde{V}_p$:

$$V_p = V_{p0} + \tilde{V}_p$$

In literature, it can be found that a way to solve this issue is direct application to the probe tip of a RF signal that is matched both in amplitude and in phase to that of the plasma, so that the RF component across the sheath is effectively removed ([19], [20]).

A very common and firmly rooted technique is to use choke filters in order to cut AC component of radio-frequency, in addition to a larger, floating compensation electrode facing the plasma, coupled with the probe and linked in parallel to the probe tip by a capacitor, necessary to drive the probe tip to follow the RF fluctuations.([21])

In this way, only DC component is collected and analysed and AC component is eliminated or in any case becomes irrelevant.

The choice of construction parameters of the probe (namely the area of the compensation electrode, and the value of the capacity connecting the latter to the probe electrode) depends on expected plasma conditions, specifically from:

- frequency of oscillation f;
- amplitude of RF oscillating component $\tilde{V}_p$.

In common applications, the lower the electron temperature T_e, the greater the error introduced by the RF component. As the expansion region of SPIDER plasma source is designed with the purpose of minimising the electron temperature, a particular care was put on the design of the compensation scheme.

In the following, an equivalent model of the probe is developed to obtain a synthetic $I-V$ characteristics; then the characteristics is analysed to estimate the error on the plasma param-

Figure 5.1: Langmuir probe components ready to be assembled.

eters that one would obtain. The analysis was carried out focusing on the effect of various C_p and $\tilde{V}_p$ values.

Costruction parameters The Langmuir probes built consist of two Molybdenum electrodes isolated and assembled with high-temperature compatible and plasma-compatible insulation materials (i.e. alumina Al_2O_3 ceramic beads and alumina glue). All the components are shown in Figure 5.1.

The main electrodes are nail-shaped with a flat head, displayed in 5.1 in the blue box. The collecting area of this electrode is the head, whose diameter is $d = 8$ mm and height is $h = 0.8$ mm. The electrode shaft is isolated with Al_2O_3 beads to the the compensation electrode, of cylindrical shape. In order to maintain insulation and allow cabling of the compensation electrode, the inner surface of the active electrode, a threaded shaft connecting to its support, is covered with Al_2O_3 glue (like the electrode in the black box in 5.1 and in Figure 5.2) and is about 3 cm long. At the end the spike is threaded in order to easy the installation of the

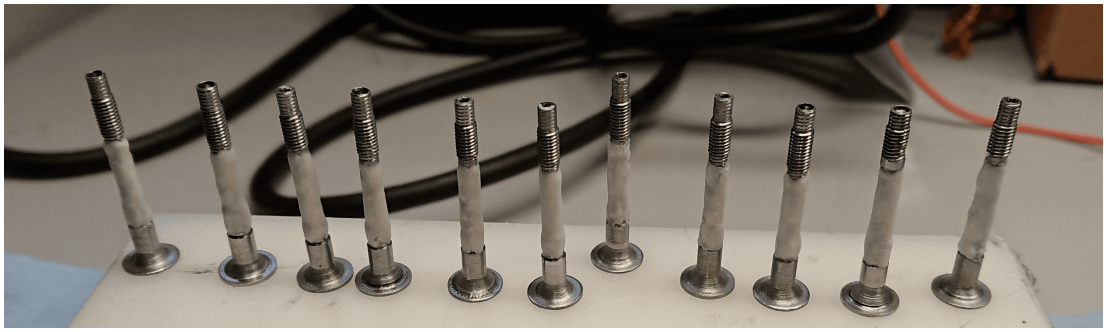

Figure 5.2: Langmuir probe main electrodes isolated with allumina ceramic glue.

Figure 5.3: Fully assembled Langmuir probe tip.

probe to its support and the linking with wires.

In the red box, one can see the compensation electrodes: they are 16 mm ($2d$) high and 8 mm diameter (d). Finally, in the green box, some allumina tubes used to isolate the two electrodes composing one probe.

In Figure 5.3 one can see a completely assembled Langmuir probe tip.

The analysis started then from an `LTSpice` model which simulated the plasma and the acquiring system as components of an electrical circuit. Two circuit models were made and compared: a DC reference, which should provide the current-voltage characteristics of an equivalent DC plasma, and a sinusoidal one, which included a fluctuation of the plasma potential at the radio frequency. They are displayed schematically in Figures 5.4, 5.5.

In Figure 5.4, $V3$ is a DC voltage generator which gives 20 V constantly; $B3$ is a tension-driven current generator which simulates the plasma. The current collected by the plasma-facing electrodes is: $I = \mathcal{A} \cdot (j_{saturation} - j_{electrons})$. For the sake of simplicity, it was assumed the simplest behaviour for the ion and electron saturation currents, that is, the collection area does not depend on the applied voltage difference $V_{plasma3} - V_{probe3}$. The following function was included in the spice model [22]:

$$I_{(DC)} = \mathcal{A}_{probe} \cdot J_{saturation} \cdot \left(1 - \frac{j_{electrons}}{j_{saturation}}\right)$$

with:

- $\mathcal{A}_{probe} = \pi(d/4)^2 + \pi dh = 7.037 \cdot 10^{-5}\mathrm{m}^2$ collecting area of the probe;
- $J_{saturation} = 0.6 \cdot n \cdot e \cdot \sqrt{\frac{eT_e}{2m_i}}$ ion saturation density of current, with T_e =1 eV and $n = 10^{17}\mathrm{m}^{-3}$;

The acquisition system for the current is modelled as a simple shunt resistor in series, schemed by $V4$ and a shunt resistance $Rshunt2$ of 10 Ω.

Regarding Figure 5.5, the plasma potential is applied through the $V1$ independent voltage source, which gives a sinusoidal signal, with a DC offset of 20 V, a frequency of oscillation of 1 MHz. In the absence of any indication about the actual $\tilde{V}_p$ in SPIDER, two cases of

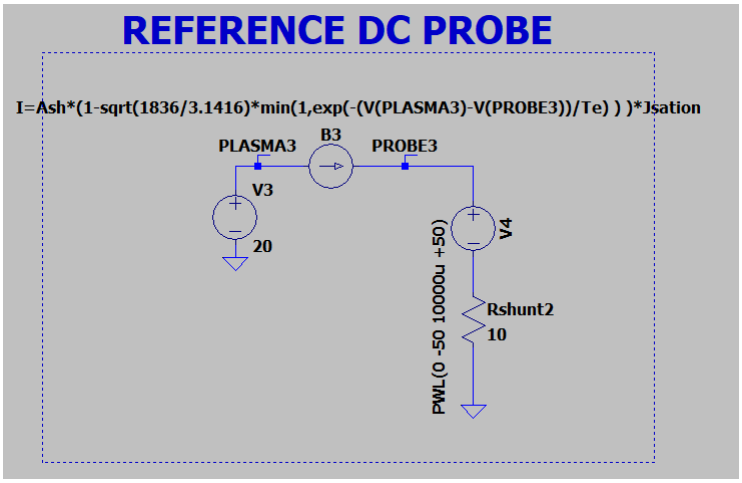

Figure 5.4: LTSpice model used for plasma simulation, DC reference.

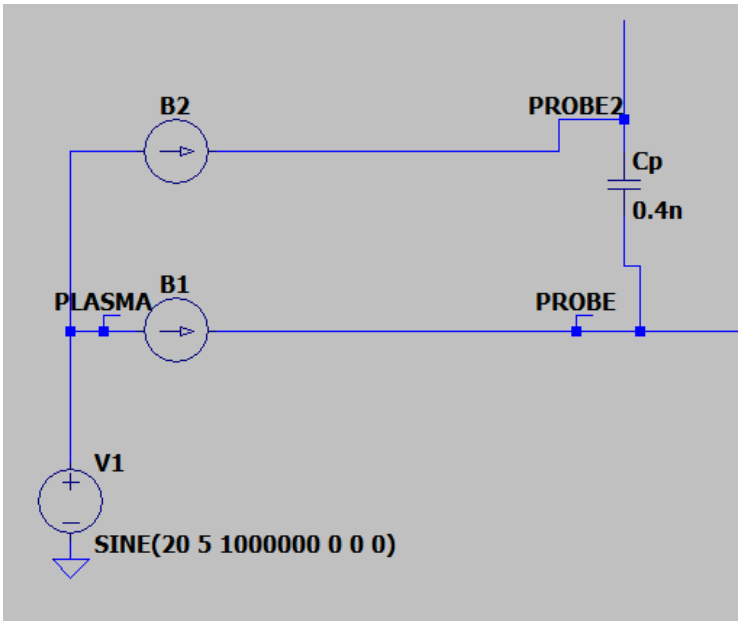

Figure 5.5: LTSpice model used for plasma simulation, AC reference.

$\tilde{V_p} = \pm 5\,\mathrm{V}$ and $\tilde{V_p} = \pm 50\,\mathrm{V}$ were studied. C_p is the variable capacity between the two electrodes, object of our analysis.

$B1$ and $B2$ are two tension-driven current generator, which are used to simulate plasma current, according to the following formulas:

$$I(B1) = \mathcal{A}_{probe} \cdot J_{saturation} \cdot \left(1 - \sqrt{\frac{m_e}{\pi m_i}} \cdot \min\left[1, \exp\left(-\frac{V_{(PLASMA)} - V_{(PROBE)}}{T_e}\right)\right]\right)$$

$$I(B2) = \mathcal{A}_{comp} \cdot J_{saturation} \cdot \left(1 - \sqrt{\frac{m_e}{\pi m_i}} \cdot \min\left[1, \exp\left(-\frac{V_{(PLASMA)} - V_{(PROBE2)}}{T_e}\right)\right]\right)$$

where:

- $\mathcal{A}_{probe} = \pi(d/4)^2 + \pi dh = 7.037 \cdot 10^{-5}\mathrm{m}^2$ is the collecting area of the probe;
- $\mathcal{A}_{comp} = 2\pi \cdot d^2 = 4.021 \cdot 10^{-4}\mathrm{m}^2$ is the area of the compensation electrode;
- $J_{saturation} = 0.6 \cdot n \cdot e \cdot \sqrt{\frac{eT_e}{2m_i}}$ is the ion saturation density of current, with $T_e = 1\,\mathrm{eV}$ and $n = 10^{17}\mathrm{m}^{-3}$;
- m_e, m_i are respectively electron and ion masses;
- $V_{(PLASMA)}, V_{(PROBE2)}, V_{(PROBE)}$ are tensions measured in the nodes indicated by Figure 5.5.

To complete the scheme, a bias generator $V2$ and a shunt resistance $Rshunt = 10\,\Omega$ are added. Two high-frequency filters (choke filters) are also included, as it is common practice in the literature (Figure 5.6).

Finally, in order to better simulate the acquisition system, a diagram of a transmission line is placed in series to the plasma, before the two filters (Figure 5.7). The complete circuit is shown in 5.8. All the parameters used are indicated in the pictures.

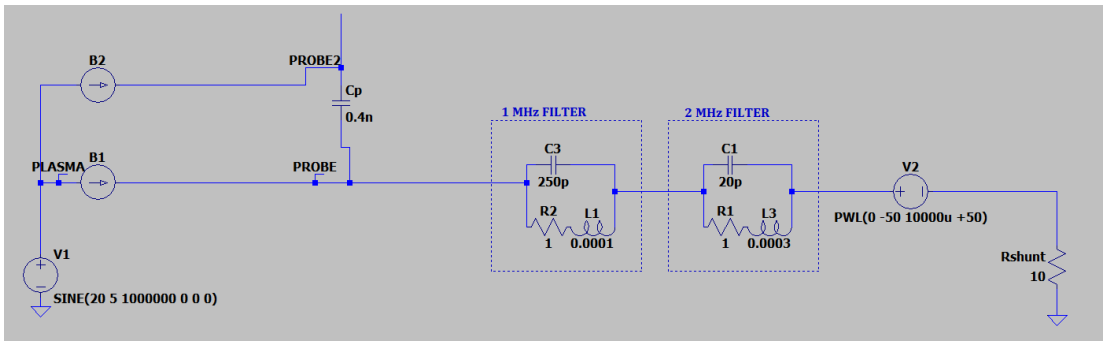

Figure 5.6: LTSpice model used for plasma simulation, with high frequency filters.

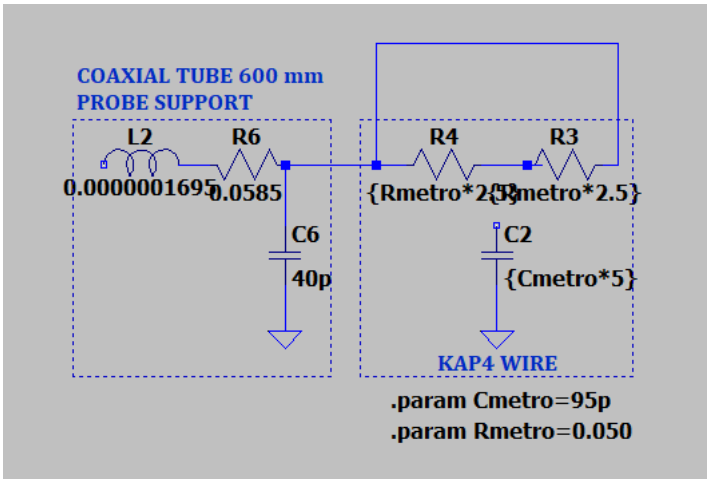

Figure 5.7: LTSpice model for the transmission line of the acquisition system.

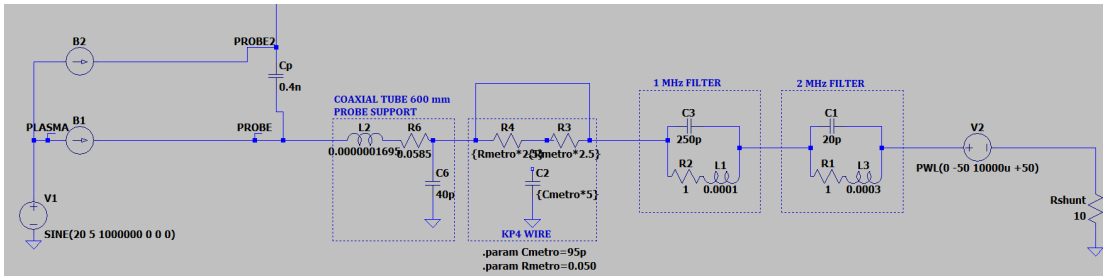

Figure 5.8: LTSpice model used for plasma simulation, with high frequency filters and transmission line.

Simulations Different simulations were made, in various configurations. The parameters which were changed were:

- capacity C_p, which assumed one of these values: 0.2 nF, 0.4 nF, 1 nF, 2 nF, 4.7 nF, 9.4 nF;
- the presence or not of the transmission line, indicated in Table 5.1 below as y=simulation with transmission line (circuit of Figure 5.8), n=without transmission line (circuit of Figure 5.8);
- the amplitude A of oscillation, either of 5 V or 50 V.

5.3 Results and discussion

Fit For each configuration discussed, the characteristic I-V curve was studied. First of all, the ion saturation regime was fitted with a straight line, so that to eliminate ion contribution to the curve. The line found was then subtracted to the original data, which were at this point fitted with a 4-parameter fit* ([16]). The parameters resulting from the fitting for each simulation are reported in Table 5.1, while in Figures 5.9, 5.10 there are some graphs by way of example.

*See 3.2: $I = 0.6 \cdot e \cdot A\sqrt{\frac{eT_e}{m_i}} \cdot n[1 + R(V_f - V)]\left[1 - \exp\left(e\frac{V-V_f}{kT_e}\right)\right]$

$\mathcal{A}$ (V)	TLine?	C_p (nF)	T_e(eV)	$n(\cdot 10^{16} m^{-3})$	V_f(V)	$R(V^{-1})$
DC Reference			1.0054	9.89767	17.161	9.5177E-09
50	y	0.2	1.9867	7.14119	12.366	5.5295E-08
50	n	0.2	1.0263	9.75658	17.146	2.5165E-09
5	y	0.2	1.0506	9.66707	17.093	6.4798E-09
50	y	0.4	1.3987	8.46992	14.837	2.2299E-08
50	n	0.4	1.0397	9.63324	17.147	2.7197E-09
5	y	0.4	0.97637	10.0144	17.1	1.3453E-08
50	y	1	1.054	9.44802	16.468	0.0003418
50	n	1	1.0723	9.52557	17.16	6.5307E-09
5	y	1	0.98228	9.95253	17.153	5.7586E-09
50	y	2	1.0327	9.73101	16.924	1.89E-09
50	n	2	1.1053	9.27599	17.156	9.1461E-09
5	y	2	0.97896	9.91499	17.135	3.9129E-09
50	y	4.7	1.0135	9.63159	17.074	2.141E-08
50	n	4.7	1.0715	9.17616	17.139	8.8894E-09
5	y	4.7	0.97859	9.77391	17.121	5.6753E-09
50	y	9.4	1.0325	9.32055	17.087	1.3793E-08
50	n	9.4	1.0795	9.02683	17.113	1.1319E-08
5	y	9.4	0.99465	9.44389	17.119	1.857E-09

Table 5.1: Results of the 4-parameter fit for each simulation considered.

Discussion The relevant parameters are T_e and n, which can be compared with the reference DC model (first row of 5.1). The goal is to understand which value of C_p provides results closer to the expected results (the results of the DC reference), as it is wished the probe to mitigate the distortion effects expected from the RF component.

By observing the tendency of both graphs, it can be assumed that whether or not a capacity is present is really influential on the estimate of both T_e and n: in fact, while T_e is overestimated if the capacity is not present, n is clearly underestimated. So it is proved that the presence of a capacity between the two electrodes of the probe is essential. The values tend to reach a balance close to DC reference very quickly, so that a little capacity of only 2 nF is enough, while increasing C_p is not particularly relevant.

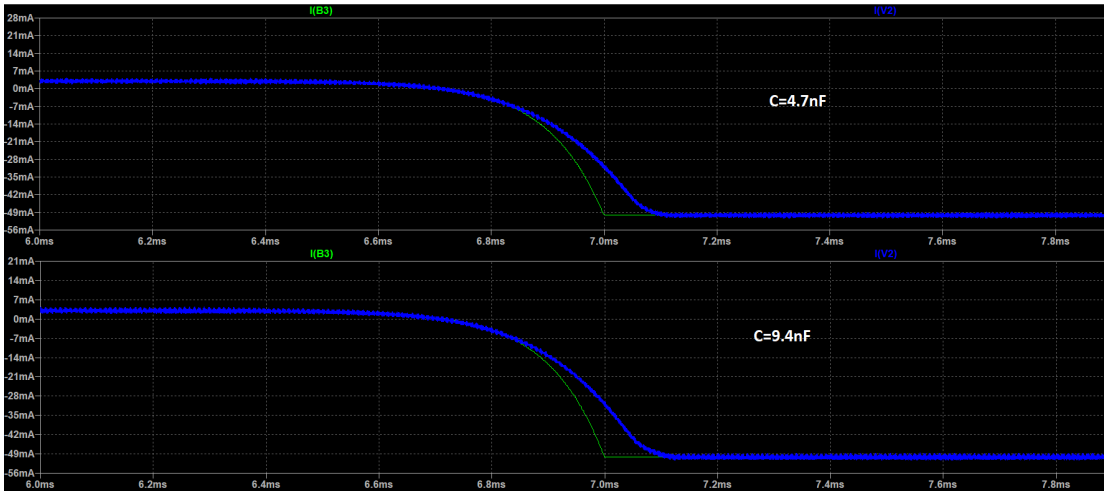

Figure 5.9: Voltage as a function of time curves for two different capacities (top: $C_p = 4.7\,\mathrm{nF}$, bottom: $C_p = 9.4\,\mathrm{nF}$). The green curve is the reference DC tension, the blue is the AC one. Both were simulated with transmission line and amplitude $\mathcal{A} = 50\,\mathrm{V}$.

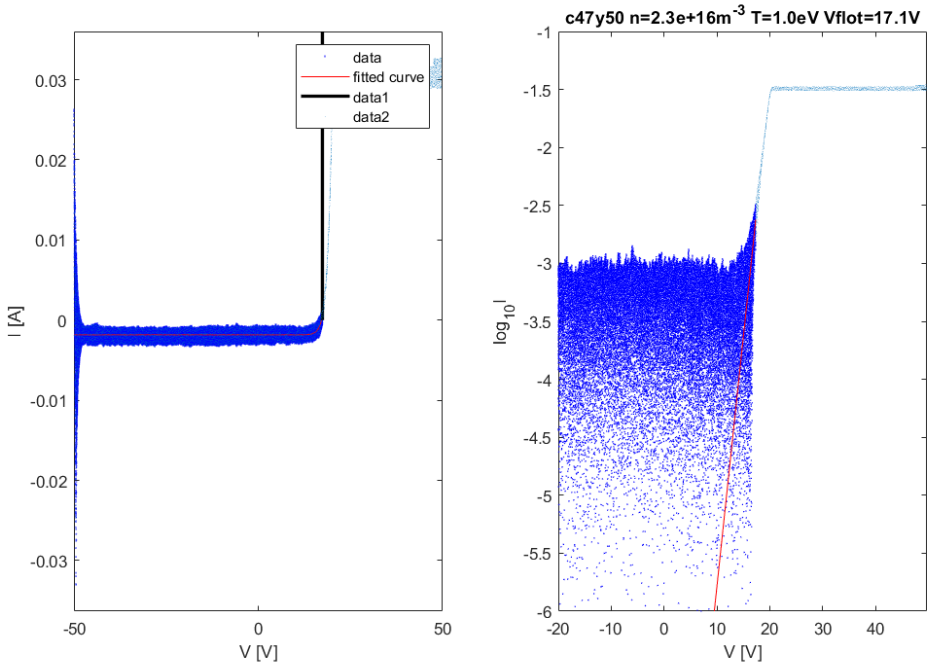

Figure 5.10: Left: I-V curve after subtracting ion saturation current with fitted line, for $\mathcal{A} = 50\,\mathrm{V}$, with transmission line and $C_p = 4.7\,\mathrm{nF}$. Right: same graph but with logarithmic scale on I-axis.

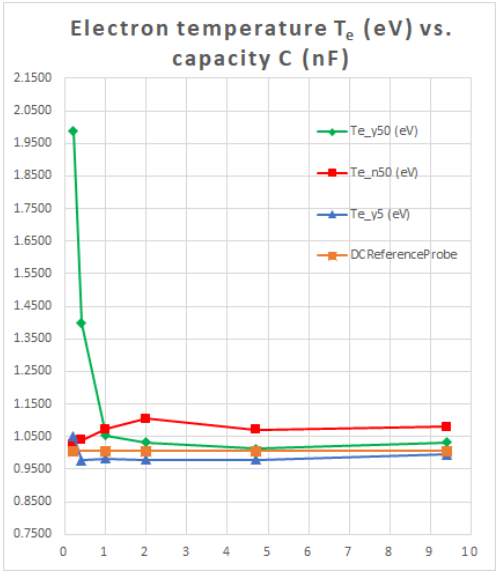

Figure 5.11: Electron temperature T_e as a function of capacity C_p. In green: simulations with transmission line and amplitude of 50 V; in red: simulations without transmission line and amplitude of 50 V; in blue: simulations with transmission line and amplitude of 5 V; in orange the DC reference.

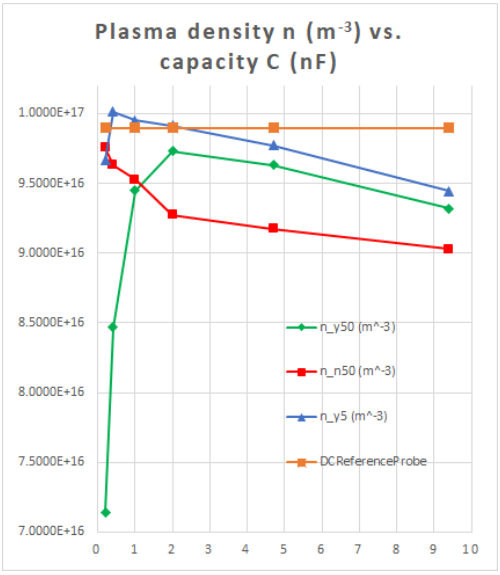

Figure 5.12: Plasma density n as a function of capacity C_p. In green: simulations with transmission line and amplitude of 50 V; in red: simulations without transmission line and amplitude of 50 V; in blue: simulations with transmission line and amplitude of 5 V; in orange the DC reference.

Conclusion In conclusion, a capacity put between the two electrodes is compulsory in order to properly estimate electron temperature and plasma density. The capacitor needs to be ceramic so as to be suitable for high temperatures and compatible with high RF frequency; in addition, the probe is required to be very compact in order to fit in the narrow space between the two electrodes. Given all of this and availability of the components, the closest capacity value is $C_p = 4.7$ nF.

A goal without a plan is just a wish.

Antoine de Saint-Exupéry

6

Project on SPIDER

In this last chapter, the details of a planning for the measures on SPIDER will be analysed.

In the final project, 4 different types of probes are present and shown in Figure 6.1:

1. 8 planar Langmuir probes, assembled as in Chapter 5 (see 5.1);
2. a double probe (ADEL), characterized in Chapter 4 (4.1);
3. a Mach probe designed as described in Chapter 3 (in particular, 3.24, 3.1);
4. 2 Compact Retarding Field Energy Analysers (RFEA probes).

Figure 6.1: All the probes used assembled on their support. The planar probes are marked with a black 1, the double probe with a blue 2, the Mach probe with a blue 3, the RFEAs with a red 4.

Figure 6.2: Wires ready for the vacuum, appropriately shielded and tinned.

6.1 Assembly and alignment

The probes are set up on top of hollow [metal] pipes, long enough to cover the whole distance between the plasma grid and the drivers. Wires, after being welded and properly shielded with Kapton tape, in order to be suitable for vacuum (Figure 6.2), could pass inside the tubes to preserve them from damages due to the plasma. Some aligning and centring devices (in Figure 6.3, b) and c)) are assembled around the probes: their role is to properly centre and align the probes when attached to the framework, as shown in 6.4 and 6.5. The framework and supports are designed so that they can hold the probes with a well-defined inclination (i.e. parallel to the ground). The centring and alignment method is very precise and employs some laser system exhibiting high accuracy.

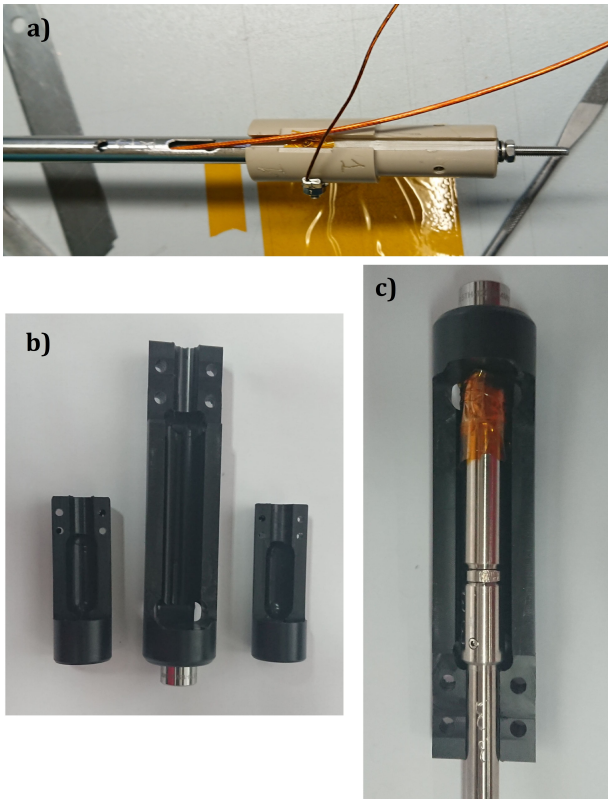

Figure 6.3: In a), a view on the end of the pole, with a wire connected passing through it. In b) the devices used for centring and alignment of the probes on the framework, one of them is assembled on one of the RFEAs and shown in c).

Figure 6.4: The framework which will be used as support inside SPIDER with two probes ready.

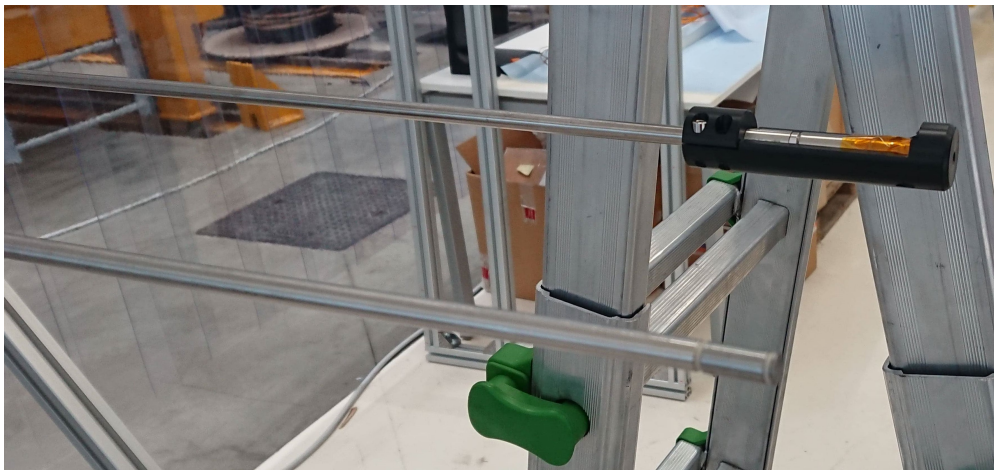

Figure 6.5: Two probes aligned mounted on the framework.

6.2 Experimental planning proposal

In the scheme reported in Figure 6.6, a proposal for the experimental campaign is reported. For each type of probe the main goals and an estimate of timing is provided.

The first step for all the probes is to get an $I - V$ characteristic curve, in order to calibrate properly the system.

Then, the main parameters are obtained, such as electron temperature, plasma density and floating potential for ADEL and the planar probes, radio frequency potential component $\tilde{V}_p$ and ion energy density function for RFEAs, and ion saturation current for the 4 electrodes in the Mach probe.

The next stage is the construction of an axial profile along z axis (Figure 1.1 for orientation): the position of the probes is changed thanks to the movable supports so that plasma parameters could be obtained as a function of the distance from the plasma grid. Possible non homogeneities are underlined, also in the vertical direction.

Finally, a more detailed analysis is conducted to thoroughly examine dependence of plasma drifts on key parameters (ADEL and Mach probe), verify connections between control parameters (RFEAs) and fully explore functionalities of the two-chamber (tandem) concept (planar probes).

Further measures could be taken by moving the Langmuir planar probes inside the drivers, by opening the vessel and repositioning them, and changing the operating gas for plasma, thus studying a different hydrogen isotope (deuterium) for more interesting comparisons.

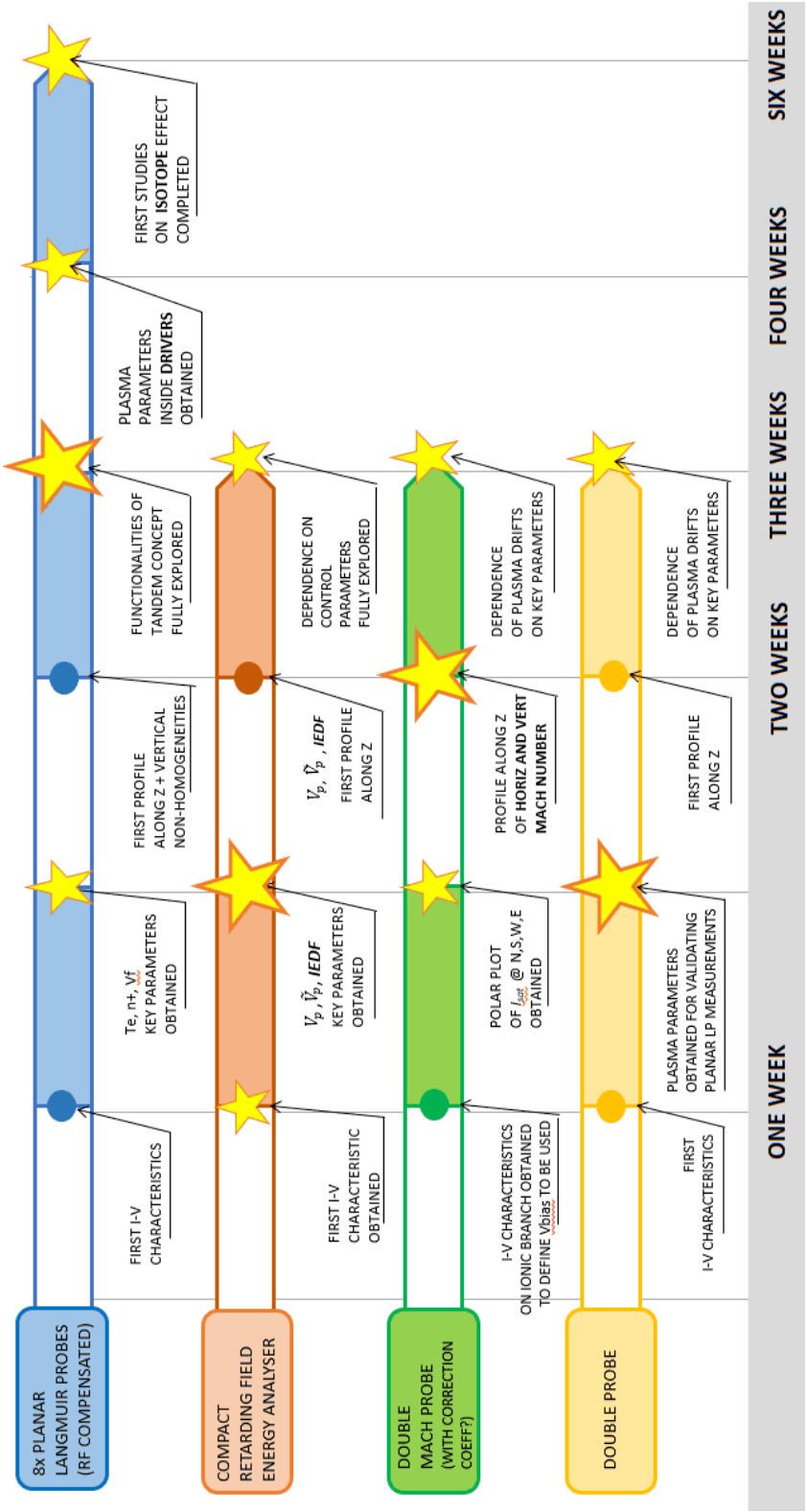

Figure 6.6: Aims and experimental duration of the proposed experimental sessions for SPIDER.

7

Conclusion

The realization of SPIDER is necessary to make the future operation of the ITER heating neutral beam injectors efficient and reliable, fundamental to the achievement of thermonuclear-relevant plasma parameters in ITER.

SPIDER's purpose, as stated in 1, is to optimize the performance of an ITER HNB-like negative ion source by maximizing the extracted negative ion current density and its spatial uniformity and by minimizing the ratio of co-extracted electrons, in order to match the ITER requirements.

The experimental study of the plasma parameters at the location of the ion extraction, and of its expansion from the driver region, is possible using Langmuir probes on mobile supports. Using these probes would give a full picture of plasma parameters, both as a function

of time and of distance from the plasma grid, which would provide complete understanding of spatial uniformity and plasma homogeneity.

In conclusion, it can be stated that each type of probe, tested or simulated, was validated. The probes should operate properly in SPIDER, reaching the goals of the experimental campaign, provided some precautions are taken.

Concerning the Mach probe:

1. being careful about the sputtering phenomenon is fundamental, as it alters the collecting area of the electrodes, hence it could heavily influence the estimate of Mach number and therefore of the velocity drift;
2. collecting at least a set of data with a 360° rotation of the probe is required to calibrate the collecting areas of the electrodes, even more importantly in SPIDER then in ATHENIS because of the higher currents and voltages involved;
3. from angular diagrams and characteristic curves the main plasma parameters could be estimated, in addition to Mach number for each direction (vertical, horizontal);
4. the direction of possible plasma drifts could be predicted if the magnetic field were well defined, which is the case of the B filter in SPIDER: the probe could be oriented so that the measure is eased.

Furthermore, regarding the double probe:

1. the probe proved to be effective in evaluating the two main plasma parameters T_e and n, however, floating potential estimate resulted more difficult and more dependent on the range of the parameters used to fit the $I - V$ curve;
2. the goal of obtaining a floating measure was fulfilled as it could be stated from the accordance between theory and experimental data. However, particular care in the installation phase (i.e. use of appropriate cables, cable shielding, and cable routing) must be taken in SPIDER to minimise parasitic capacities and induced currents, given the much longer path the cables must follow;
3. it cannot be assured that the two electrodes are perfectly symmetrical, so the fit without the $\alpha = 1$ approximation (see 4.2) is more appropriate and considers also eventual plasma asymmetries.

Finally, for the planar Langmuir probes:

1. the ceramic capacitor introduction between the two electrodes (the main and the compensation one) cleans the signal and allows proper analysis, even though its value is not the optimum one but the closest available;

2. the study of the $I - V$ characteristic curve of the 8 probes, positioned in different points of the plasma, could give a good scan of the plasma parameters as a function of the distance from the plasma grid, considering also eventual vertical drifts and other phenomena that could occur;

3. by changing their position, both the expansion chamber and the drivers plasmas could be studied and characterized;

4. more sets of data could be collected after changing discharge gas (from hydrogen to deuterium), which would give further information;

5. dependence of plasma parameters on bias potential, B filter and RF power could also be studied in detail.

References

[1] V. Toigo et al., "The PRIMA test facility: SPIDER and MITICA test-beds for ITER neutral beam injectors," *New Journal of Physics*, vol. 19, no. 8, aug 2017. [Online]. Available: https://doi.org/10.1088%2F1367-2630%2Faa78e8

[2] D. Marcuzzi, P. Agostinetti, M. Dalla Palma, F. Degli Agostini, M. Pavei, A. Rizzolo, M. Tollin, and L. Trevisan, "Detail design of the beam source for the spider experiment," *Fusion Engineering and Design*, vol. 85, no. 10-12, pp. 1792–1797, december 2010. [Online]. Available: https://doi.org/10.1016/j.fusengdes.2010.05.039

[3] M. Bacal, "Physics aspects of negative ion sources," *Nuclear Fusion*, vol. 46, no. 6, pp. S250–S259, may 2006. [Online]. Available: https://doi.org/10.1088%2F0029-5515%2F46%2F6%2FS05

[4] M. Kuriyama et al., "Operation of the negative-ion based NBI for JT-60U," *Fusion Engineering and Design*, vol. 39-40, pp. 115–121, september 1998. [Online]. Available: https://doi.org/10.1016/S0920-3796(98)00183-5

[5] N. Hershkowitz, "How langmuir probes work," in *Plasma Diagnostics. Discharge Parameters and Chemistry*, 1st ed., O. Auciello and D. L. Flamm, Eds. 1250 Sixth Avenue, San Diego, CA 92101: Academic Press, Inc., 1989, vol. 1, ch. 3, pp. 113–183.

[6] P. C. Stangeby, "The interpretation of plasma probes for fusion experiments," in *Plasma Diagnostics. Surface analysis and Interactions*, 1st ed., O. Auciello and D. L.

Flamm, Eds. 1250 Sixth Avenue, San Diego, CA 92101: Academic Press, Inc., 1989, vol. 2, ch. 5, pp. 170–185.

[7] U. Fantz, L. Schiesko, and D. Wünderlich, "Plasma expansion across a transverse magnetic field in a negative hydrogen ion source for fusion," *Plasma Sources Science and Technology*, vol. 23, no. 4, p. 044002, jul 2014. [Online]. Available: https://doi.org/10.1088%2F0963-0252%2F23%2F4%2F044002

[8] L. Schiesko, P. McNeely, P. Franzen, U. Fantz, and NNBI-Team, "Magnetic field dependence of the plasma properties in a negative hydrogen ion source for fusion," *Plasma Physics and Controlled Fusion*, vol. 54, no. 10, p. 105002, aug 2012. [Online]. Available: https://doi.org/10.1088%2F0741-3335%2F54%2F10%2F105002

[9] P. McNeely, B. Heineman, W. Kraus, R. Riedl, E. Speth, and O. Vollmer, "Langmuir probe studies on a RF ion source for NBI," *Fusion Engineering and Design*, vol. 56-57, pp. 493–498, october 2001. [Online]. Available: https://doi.org/10.1016/S0920-3796(01)00332-5

[10] B. Crowley, D. Homfray, S. Cox, D. Boilson, H. de Esch, and R. Hemsworth, "Measurement of the electron energy distribution function by a langmuir probe in an ITER-like hydrogen negative ion source," *Nuclear Fusion*, vol. 46, no. 6, pp. S307–S312, may 2006. [Online]. Available: https://doi.org/10.1088%2F0029-5515%2F46%2F6%2FS11

[11] M. Bandyopadhyay, A. Tanga, H. D. Falter, P. Franzen, B. Heinemann, D. Holtum, W. Kraus, K. Lackner, P. McNeely, R. Riedl, E. Speth, and R. Wilhelm, "Analysis of plasma dynamics of a negative ion source based on probe measurements,"

Journal of Applied Physics, vol. 96, no. 8, pp. 4107–4113, 2004. [Online]. Available: https://doi.org/10.1063/1.1787619

[12] D. Wünderlich, L. Schiesko, P. McNeely, U. Fantz, P. Franzen, and NNBI-Team, "On the proton flux toward the plasma grid in a RF-driven negative hydrogen ion source for ITER NBI," *Plasma Physics and Controlled Fusion*, vol. 54, no. 12, p. 125002, nov 2012. [Online]. Available: https://doi.org/10.1088%2F0741-3335%2F54%2F12%2F125002

[13] M. Fadone, V. Antoni, D. Aprile, G. Chitarin, A. Fassina, E. Martines, G. Serianni, E. Sartori, F. Taccogna, and M. Zuin, "Plasma characterization of a hall effect thruster for a negative ion source concept," *AIP Conference Proceedings*, vol. 2052, no. 1, p. 020009, 2018. [Online]. Available: https://aip.scitation.org/doi/abs/10.1063/1.5083727

[14] I. H. Hutchinson, *Principles of Plasma Diagnostics*, 2nd ed. The Edinburgh Building, Cambridge CB2 2RU, UK: Cambridge University Press, 2002.

[15] K. S. Chung, "Mach probes," *Plasma Sources Science and Technology*, vol. 21, no. 6, p. 063001, nov 2012. [Online]. Available: https://doi.org/10.1088%2F0963-0252%2F21%2F6%2F063001

[16] D. Desideri and G. Serianni, "Four parameter data fit for langmuir probes with nonsaturation of ion current," *Review of Scientific Instruments*, vol. 69, no. 6, pp. 2354–2356, 1998. [Online]. Available: https://doi.org/10.1063/1.1148942

[17] C. Poggi et al., "CRISP: the compact RF ion source prototype for emittance scanner testing," *Review of Scientific Instruments*, Submitted.

[18] A. Boschi and F. Magistrelli, "Effect of a r.f, signal on the characteristic of a langmuir probe," *Il Nuovo Cimento (1955-1965)*, vol. 29, no. 2, pp. 487–499, Jul 1963. [Online]. Available: https://doi.org/10.1007/BF02750367

[19] N. S. J. Braithwaite, N. M. P. Benjamin, and J. E. Allen, "An electrostatic probe technique for RF plasma," *Journal of Physics E: Scientific Instruments*, vol. 20, no. 8, pp. 1046–1049, aug 1987. [Online]. Available: https://doi.org/10.1088%2F0022-3735%2F20%2F8%2F018

[20] V. A. Godyak and R. B. Piejak, "Probe measurements of the space potential in a radio frequency discharge," *Journal of Applied Physics*, vol. 68, no. 7, pp. 3157–3162, 1990. [Online]. Available: https://doi.org/10.1063/1.346389

[21] I. D. Sudit and F. F. Chen, "RF compensated probes for high-density discharges," *Plasma Sources Science and Technology*, vol. 3, no. 2, pp. 162–168, may 1994. [Online]. Available: https://doi.org/10.1088%2F0963-0252%2F3%2F2%2F006

[22] M. A. Lieberman and A. J. Lichtenberg, *Principles of Plasma Discharges and Materials Processing*, 2nd ed. Hoboken, New Jersey: John Wiley and Sons, Inc., 2005.